Bulletin 137

INTERPRETATIONS AND GENESIS OF CRETACEOUS AGE VEINS AND EXPLORATION POTENTIAL FOR THE EMERY MINING DISTRICT, POWELL COUNTY, MONTANA

Stanley L. Korzeb,[1] Kaleb C. Scarberry,[1] and Jarred L. Zimmerman[2]

[1]Montana Bureau of Mines and Geology, Butte, Montana

[2]Broadway Gold Mining LCD, Vancouver, British Columbia

MBMG
Montana Bureau of Mines and Geology

Cover photo: Emery mill and mine dumps. Photo by Stanley Korzeb, MBMG.

Bulletin 137

INTERPRETATIONS AND GENESIS OF CRETACEOUS AGE VEINS AND EXPLORATION POTENTIAL FOR THE EMERY MINING DISTRICT, POWELL COUNTY, MONTANA

Stanley L. Korzeb,[1] Kaleb C. Scarberry,[1] and Jarred L. Zimmerman[2]

[1]Montana Bureau of Mines and Geology, Butte, Montana

[2]Broadway Gold Mining LCD, Vancouver, British Columbia

CONTENTS

FIGURES

TABLES

Plate 1 is included in the back pocket.

INTRODUCTION

The Emery mining district was chosen for this investigation because the district may have potential for undiscovered resources such as a deep porphyry or stockwork deposit. Elliott and others (1993) gave the district a moderate potential for the occurrence of a porphyry or stockwork copper–molybdenum deposit based on favorable geologic conditions for the occurrence of undiscovered resources. Past mining produced gold, silver, copper, lead, and zinc from epithermal/mesothermal quartz veins. From investigations of other mining districts, epithermal vein systems can be linked to porphyry systems such as those found in the Butte district and the Philippines (Chang and others, 2011; Cooke and Bloom, 1990; Rusk and others, 2008a; Sillitoe, 2010).

Exploration for new mineral deposits often requires focusing on past producing mining districts such as the Emery mining district for overlooked mineral deposits and exploration targets. Overlooked mineral deposits and new exploration targets can be extensions of known mineral resources or related to mineralizing fluid sources associated with, for example, unrecognized deep porphyry systems. Locating extensions of known mineral deposits or mineralizing fluid sources requires an understanding of the genesis of past and present producing mining districts.

The goal of investigating these mining districts is to update past studies with newly generated data. New data are generated by advanced investigative techniques including stable isotope geochemistry, trace element and whole rock geochemistry, age dating, identifying alteration sequences, mineralogy, fluid inclusion studies, and if available, geophysical data. By using these techniques to expand the data generated from past investigations, it is possible to determine the origin of mineral resources with historic production. From the data generated, an ore deposition model can be constructed for the mining district that can be used as an exploration tool to locate potential exploration targets.

METHODS

Methods used for this investigation consisted of sampling dumps and stockpiles of the existing mines and outcrops, because existing underground workings were caved and inaccessible. Samples were analyzed for alteration types, fluid inclusions, stable isotopes, mineralogy, and trace element and whole-rock geochemistry. A granodiorite intrusion was dated by U/Pb methods from zircon. Altered host rock was dated by $^{40}Ar/^{39}Ar$ methods from sericite. This information was used to construct a geologic model for the district and assess the exploration potential for possible resources.

PREVIOUS INVESTIGATIONS

The geology and mines of the Emery mining district were first described by Pardee and Schrader (1933). They visited the district in 1926, met with the mine operators, and entered some of the underground mines. After Pardee and Schrader (1933), several theses and professional reports were published. The first was a thesis by Elliott (1939) on the geology and mineralogy of the Emery mine. Stejer (1948) completed a thesis on the Bonanza mine describing the geology, mineralogy, genesis, and economic future for the mine. Callaway (1950) investigated the mineralization of the Bonanza mine and expanded on the work completed by Stejer (1948) by examining the mineral paragenesis and recognizing different mineralizing stages. Joyce (1951) described the mineralogy, mineral paragenesis, and economic potential of the Black-Eyed May, Emma Darling, Argus, and Hidden Hand mines located in the northern part of the district. Robertson (1953) published a memoir on the geology and mineral deposits and additional data on the geology, mineralogy, genesis, and descriptions of all the major mines.

In the 1980s, a number of mining companies investigated the district for disseminated gold deposits. These investigations generated unpublished company reports, correspondence, and maps that are archived at the Montana Bureau of Mines and Geology (MBMG). During this same time, Al-Khirbash (1982) completed a M.S. thesis summarizing data he obtained from a deep core hole, expanding upon the geology, alteration, mineralogy, and origin of the mineralization. Derkey (1986) also completed a geologic map of the district and updated the geologic and structural interpretations. Zimmerman (2016) completed a thesis on the district, updating previous investigations with isotope, fluid inclusion, and mineralogical data.

HISTORY

When first established in the 1870s, the Emery district was known as the Zosell mining district. The district was originally named after W.T. Zosel, who located the Bonanza lode (plate 1), and was a promi-

nent rancher and homesteader living in the area. Because of a misspelling of the Zosel name, “Emery Mine” was also used as an early name on the basis of the Emery mine being the largest mine in the district. Emery became the preferred district name (Derkey, 1986).

Mining activity began in 1872 with the discovery of placer gold in Rocker gulch (plate 1) by H.L. Hoffman (Callaway, 1950). After this discovery, placer operations were also carried out in Spring and Deep Gulches and a small tributary of Little Cottonwood Creek (Robertson, 1953). Total placer mining production is reported by Robertson (1953) to be about 3,628 oz, or $75,000 (based on the late 1800s gold price of $20.67). Placer mining led to the discovery of lode deposits by the late 1800s (Callaway, 1950).

Joe Peterson discovered the first lode deposit in 1887 at the site of the Hidden Hand claim (Derkey, 1986). A year later, John Renault discovered what became the Emery lode, which was later staked as the Carbonate Hill lode by W.C. Emery. During the early years, between 1891 and 1905, there was a high rate of development and production. W.T. Zosel discovered the Bonanza lode in 1895, one of the largest veins in the district. By 1905, all the principal lode deposits were discovered, including the Blue Eyed Maggie, Argus, and Emma Darling (plate 1; and Robertson, 1953).

Activity slackened from 1908 to 1909, with little mining taking place until the late 1930s (Robertson, 1953). The second stage of mining activity was interrupted by World War II. Gold mining was shut down during the war years because gold mining did not support the war effort, and mining equipment became unobtainable for gold mines (Robertson, 1953). After the war, the high price of lead kept the mines in production until the recession of 1949 started driving up the cost of labor and materials. By 1950, the operating mines started closing, and by 1951 all mining ended. The Hidden Hand was the last mine to close (Robertson, 1953).

Emery Mine

Most of the known early mining history centers on events at the Emery mine, one of the most important mines and the largest past producer. After W.C. Emery staked the Emery mine, he developed the vein to a depth of 100 ft on a decline and sold the property to Conrad Kohrs and others in 1890 (Robertson, 1953; Elliott, 1939). Three years after acquiring the mine, Kohrs patented the Carbonate Hill claim and adjacent claims. The mine was successfully operated until 1902 when Kohrs sold it to the Emery Mining Company. Under the direction of the Emery Mining Company, operations continued producing gold, silver, and lead for the next 5 years, with a total reported value of $90,000. Deer Lodge Consolidated Mines Company Limited gained control of the mine in 1907. To gain better access to the underground workings, the new owners engaged in extensive development that included sinking a vertical shaft north of the decline. The new development of the underground mine workings, in conjunction with insufficient production, bankrupted the Deer Lodge Consolidated Mining Company (Robertson, 1953).

From 1908 to 1910, the property was inactive until the previous Emery Mining Company formed a new company named the Emery Consolidated Mining Company and took control of the property (Robertson, 1953; Elliott, 1939). In 1923, electricity was bought to the mine and a 70 ton-per-day flotation mill was constructed. In spite of these efforts, there was little production until 1935, when 12,000 tons of ore was processed. From 1936 to 1939, mining activity was limited to additional development and ore was hand sorted for shipment. In 1945, John B. White constructed a 100-ton-per-day flotation mill, which was operated by the Deer Lodge Mining Company for the next 3 to 4 years. The mill treated 8,968 tons of ore over a 2-year period. By 1950, the Emery mine was closed due to the high cost of labor and materials (Robertson, 1953).

District Production

McClernan (1976) reported on production from 1902 and ending in 1966 (table 1). There are no accurate production records prior to 1902. After 1951, when the last mine closed, a minor amount of ore was produced, consisting of 106 tons that yielded 4 oz gold, 1,382 oz silver, 14,700 pounds lead, and 3,100 pounds zinc. Because all the mines were closed after 1951, limited production from 1952 to 1966 was from stockpiled ore and handpicked from dumps.

Table 1. Emery mining district production from 1902 through 1966 (McClernan, 1976).

Ore	95,151 tons
Gold	31,382 oz
Silver	865,980 oz
Lead	2,389,754 lb
Zinc	693,947 lb
Copper	42,974 lb

Production in the district peaked from 1947 to 1948 when the Bonanza mine shipped 1,853 tons of ore that yielded 686 oz of gold and 3,569 oz of silver, with a calculated grade of 0.37 oz/t gold and 1.9 oz/t silver. The Bonanza mine also shipped 71 tons of lead ore that yielded 8 oz gold, 1,800 oz silver, 141 lbs copper, 36,630 lbs lead, and 7,684 lbs zinc (Derkey, 1986). Calculated grade for the 71 tons of ore from the Bonanza mine was 0.11 oz/t gold, 25 oz/t silver, 0.09% copper, 26% lead, and 5.4% zinc. Based on total production records, the average grade calculated for ore shipped from the district was 0.33 oz/t gold, 9.1 oz/t silver, 1.3% lead, 0.36% zinc, and 0.02% copper.

Recent Exploration History

After the 1950s, most activity in the Emery mining district centered on exploration by a number of mining companies searching for shallow, large-tonnage, precious metals deposits or for deep-seated porphyry–copper deposits. The following summary of exploration activity starting in the 1960s is taken from unpublished company reports and correspondence archived at the MBMG.

In 1969, Placer Amex Corporation drilled two core holes and 20 rotary holes in the northern part of the district, searching for a shallow gold deposit that could be mined by open-pit methods. Placer Amex Corporation did not continue with their exploration program and left the area by the 1970s.

Gulf Mineral Resources drilled two holes in the northern part of the district searching for a deep-seated porphyry deposit. The first hole was drilled in 1976 near the Hidden Hand mine and reached a total depth of 2,903 ft. In 1978, another hole was drilled to a total depth of 1,965 ft, east of the Emma Darling patented claim. Al-Khirbash (1982) logged and described the deeper hole and reported the results as part of his Master of Science thesis.

After Gulf Mineral Resources' drilling efforts, Lacana Corporation started an exploration program in the vicinity of the Hidden Hand and Argus mines in 1982. Their exploration efforts consisted of a surface sampling and drilling program. The first phase was an exploration geochemistry program consisting of 296 rock samples, 50 dump samples, and 47 soil samples. In the early 1980s, the underground workings of the Argus and Hidden Hand mines were still accessible, allowing 48 rock samples to be taken from these workings. Following the exploration geochemistry program, a drilling program commenced consisting of eight rotary holes. Lacana concluded that potential economic gold resources are present in the Hidden Hand vein and continue to the Bonanza mine to the south. They also determined the dumps of the Argus and Hidden Hand mines have economic potential for gold recovery.

While Lacana Corporation was engaged in their exploration program, there was renewed activity at the Emery mine. Derkey (1986) reported that Emery Mining Associates constructed a 200 ton-per-day mill in the early 1980s at the site of the lower vertical shaft. The mill produced approximately 100 tons of concentrate using ore from the Emery mine that was later shipped to the East Helena smelter. Even though the mill operated successfully, low metals prices caused it to close. In 2016, the mill is still present but remains closed.

Exxon Corporation took an interest in the district in 1985 and began searching for a shallow gold resource that could be mined by open-pit methods. Exxon explored the district using surface sampling, a geophysical survey, and a drilling program. The geophysical survey was conducted from 1985 to 1986 and consisted of induced polarization (IP) and spectral polarization (SP) in selected areas. Geophysical and surface sampling anomalies were tested by a drilling program that consisted of 14 reverse circulation and 4 core holes. Four drill holes revealed potential for a gold resource that was flat-lying and could be exploited by open-pit mining. After this discovery, Exxon Corporation began seeking to joint venture the project.

Freeport-McMoRan Corporation (FMC) joint ventured with Exxon Corporation in 1986 and continued the exploration program. At the same time, FMC included Montana Precision Mining, Ltd. (formerly Emery Mining Associates) and Hiko-Bell in the joint venture agreement. FMC started their exploration program in 1986 with a geophysical survey consisting of ground magnetics, regional aerial magnetics, very low frequency-ground magnetometer (VLF), IP, and SP. By 1987, FMC was conducting a surface sampling, geophysical, and drilling program in the northern half of the district and in the vicinity of the Bonanza mine. Most work centered on exploring the Hidden Hand, Emma Darling, and Bonanza veins. Exploration consisted of 72 core and 17 reverse circulation holes, two trenches, and a VLF survey. In 1989, FMC defined potential for a 150,000 oz gold resource in the northern area of the district and 50,000 oz of gold in the Bonanza area.

During the joint venture with FMC, Montana Precision Mining was doing exploration on their property in the southern part of the district. From 1985 to 1986,

an SP and IP geophysical survey was conducted in the Carbonate Hill area, which encompassed the Emery mine. Montana Precision Mining also conducted exploration activities to define a low-grade gold deposit in the vicinity of the Bonanza mine and the Bell patented mining claim. The exploration activities included a trenching program, a reverse circulation drilling program, and a geophysical survey. Results of this exploration program delineated an indicated gold resource of 218,000 tons containing 28,262 oz of gold and 366,714 oz of silver. At the Emery mine, 57,941 tons of ore is inferred to remain in the underground workings, which might contain 21,553 oz of gold and 891,711 oz of silver. The dumps at the Emery mine are estimated to have 35,859 tons of ore, which contains 4,303 oz of gold and 153,476 oz of silver.

FMC judged the gold resource too small to be profitable and ended the joint venture agreement in 1989. U.S. Minerals Exploration Co. acquired the FMC properties in 1990 and entered into a three-way joint venture agreement with Montana Precision Mining and Hecla Mining Corporation. From 1991 to 1992, Hecla drilled a total of 82 holes and completed the ground magnetics survey started by FMC. This exploration activity took place in the vicinity of the Hidden Hand and Bonanza mines and other potential resource areas. Results of this exploration effort further defined the Bonanza deposit, which is estimated to have 207,000 tons of ore containing 27,000 oz of gold with a grade of 0.132 oz gold per ton and a cutoff grade of 0.050 oz gold per ton.

Hecla ended the project in the 1990s and Montana Precision Mining started looking for another joint venture partner. Most exploration and mining activity in the district ended at this time and the district remained idle. Some of the patented claims were sold as potential house lots. Montana Precision Mining planned to renew mining activity in 2014 by evaluating the remaining mine dumps and stockpiled ore at the Emery and Bonanza mine sites as a possible gold and silver resource (F. Foster, oral commun., 2014).

REGIONAL GEOLOGY

Precious metal ore deposits formed throughout the western United States during Mesozoic assembly of the North American Cordillera (Hildebrand, 2013). Numerous plutons were intruded into an evolving thrust wedge in northern Idaho and western Montana (summary in Lageson and others, 2001). The Boulder Batholith, and co-magmatic Elkhorn Mountains Volcanics (EMV), represent an exceptionally well preserved and voluminous example of Cordillera arc magmatism in western Montana (Rutland and others, 1989).

Field relationships indicate the Boulder Batholith was emplaced into EMV lavas and ignimbrites between 85 and 76 Ma (Tilling and others, 1968; Mahoney and others, 2015). U/Pb zircon ages for the Butte Granite, the main pluton by volume of the Boulder Batholith, are 74.5 ± 0.9 Ma (Lund and others, 2002) and 76.28 ± 0.14 Ma (Martin and others, 1999). Olson and others (2016) report $^{40}Ar/^{39}Ar$ ages that range from 84.7 to 83.7 Ma for a 950-m section of EMV ignimbrites south of Boulder, Montana.

The Boulder Batholith crystallized at a depth of 6 to 9 km (3.7 to 5.6 mi), based on aluminum-in-hornblende barometry studies from the Butte mining district (Houston and Dilles, 2013). The EMV formed a volcanic plateau 4.6 km (2.06 mi) thick over the batholith (Smedes, 1966). Exhumation and erosion of the continental magma system occurred in response to extensional collapse of the Cordilleran Foreland Fold and Thrust Belt (Constenius, 1996) from 49 to 20 Ma, followed by Basin and Range block faulting since 15 Ma (Reynolds, 1979).

DISTRICT GEOLOGY

Polymetallic veins in the Emery mining district occur in basalt–andesite lavas of the lower member of the EMV on the west flank of the Boulder Batholith (plate 1). Most vein-host lavas are altered and difficult to classify. Pardee and Schrader (1933) described vein host lavas as andesites, and Derkey (1986) mapped them as dark gray, porphyritic basalt with plagioclase phenocrysts, and medium green, porphyritic basalt with pyroxene phenocrysts. Major and trace element geochemistry of less altered lavas shows they are high-K, basalt–andesites and andesites (Scarberry, 2016). Vein networks may, in part, have formed along vesicular rubble zones in lower member lavas (Robertson, 1953; Derkey, 1986) and/or are aligned with N–S-striking thrust fault systems (Ruppel, 1961) and related steeply dipping E–W-striking tear faults (Robertson, 1953).

Lower member andesites formed during fissure eruptions (Klepper and others, 1957) that filled and overflowed the edges of a broad N. 35° E.-trending, regional synclines (Smedes, 1966). EMV rocks south of the Emery mining district (plate 1) include fissure dikes, breccia, and lava flows (Scarberry, 2016), similar in texture and mineralogy to lavas described by previous studies in the Emery mining district (Derkey, 1986).

Five kilometers (3.1 mi) south of the district 400 m of middle member EMV rhyolite ignimbrite and intercalated tuff breccia is banked into lower EMV basalt–andesite lavas. The ignimbrite is essentially missing and <5 m thick where exposed in the Emery mining district. The disparity in thickness of the middle member EMV rhyolite ignimbrite over a short distance led Scarberry (2016) to map its contact with EMV basalt–andesite lavas as a caldera wall (see plate 1 and cross section).

The intrusive contact between Butte granite and the lower EMV basalt–andesite lavas is essentially concordant near the Emery mining district (Robertson, 1953; Scarberry, 2016). Emplacement of the Butte granite thermally metamorphosed and deformed EMV basalt–andesite lavas. The lavas are locally cooked to hornfels, and cut by a network of quartz veins near their contact with Butte granite in the southern part of the Sugarloaf Mountain 7.5' quadrangle (Scarberry, 2016). The lavas exhibit gentle, open folds that plunge 15° northeast (Scarberry, 2016). Emplacement of the granite may have formed flexure in the basalt–andesite lavas that provided channel ways for ore-bearing solutions (Robertson, 1953).

Granodiorite intrusions of uncertain origin occur in the district. A granodiorite intrusion was mapped near the Hidden Hand mine in 1983 for Lacana Mining Inc. and was reported in an unpublished company report by U.S. Minerals Exploration Co. archived at the MBMG. A sample for thin sections and age dating of the granodiorite was collected from a trench excavated along the intrusion. Petrographic examination reveals the presence of biotite and plagioclase phenocrysts with a fine-grained groundmass of quartz and plagioclase. Magnetite and zircon occur as accessory minerals. The granodiorite was partially altered, with sericite replacing plagioclase along fractures and chlorite replacing biotite. Granodiorite described by Scarberry (2016) is within vertically oriented beds of Cretaceous metasedimentary rocks in a steeply dipping shear zone in the Sugarloaf Mountain 7.5' quadrangle.

GEOCHRONOLOGY

Zircons from the granodiorite exposed in the Emery mining district and volcanic rocks from the Sugarloaf Mountain quadrangle were dated at the Boise State University Isotope Geology Laboratory. Conventional density and magnetic methods were used to separate the zircon crystals from the granodiorite hand sample. The zircon separate was annealed in a muffle furnace at 900°C for 60 h. After annealing, individual zircon crystals were selected, mounted, polished, and imaged by cathodoluminescence (CL) on a scanning electron microscope. From the CL images, 41 locations for spot analysis by laser ablation-inductively coupled plasma mass spectrometry (LA-ICP-MS) were selected. LA-ICP-MS analysis utilized an X-Series II quadrupole ICP-MS and New WaUp-213 Nd:YAG UV (213 nm) laser ablation system. An external standard AUSZ2 was used during the analytical session (Rivera and others, 2013; Kennedy and others, 2014).

Zircons extracted from the granodiorite are equant to elongated, weakly luminescent and oscillatory zoned (fig. 1). Many crystals have a thin (a few micrometers thick), highly luminescent rim that could be a cryptic record of minor recrystallization. The 41 spot analysis yielded a normal distribution with a weighted mean $^{207}Pb/^{206}Pb$ date of 1,777 ± 8 (20) Ma. Excluding ten analyses with discordance >5%, and equivalent weighted mean $^{206}Pb/^{238}U$ date of 1,771 ± 17 (25) Ma is obtained. Results suggest a Paleoproterozoic crystallization age for the zircons that are therefore shown to be xenocrysts in the granodiorite.

Veins in the Butte mining district, epithermal veins of the Cruse (Belmont) mine, and skarn/replacements of the New World mining district appear to be genetically related to porphyry systems and range in age from Late Cretaceous through Eocene (Foster and Childs, 1993; Houston and Dilles, 2013). Scarberry (2016) mapped Eocene dikes that appeared to follow N–S-trending Cretaceous faults (diorite in fault is 79.8 Ma and is deformed). Zircons from one diorite dike and two EMV samples were dated by U-Pb methods and give an age of 77.4 ± 0.8 (1.7) and 78.5 ± 1.6 (2.2) Ma for EMV and 79.8 ± 1.1 (1.9) Ma for diorite. Results of the zircon dates are in table 2; sample descriptions are in appendix A.

Granodiorite adjacent to the vein extension from the Hidden Hand mine (sample point 14 on plate 1) was sericiticly altered at the same time as the volcanic rocks. Sericite from granodiorite altered during vein development yielded an $^{40}Ar/^{39}Ar$ date of 77.93 ± 0.30 Ma with an error of <0.10 Ma. Analysis of the sample was conducted at the Oregon State University Argon Geochronology Laboratory, Corvallis, Oregon. Analysis was completed by standard incremental heating at 77-s intervals using an Argus-VI-D instrument yielding a weighted plateau of 77.93 ± 0.20 Ma. This date is equivalent to the Cretaceous age dates from the EMV rhyolite ash flow tuff units and diorite intrusion.

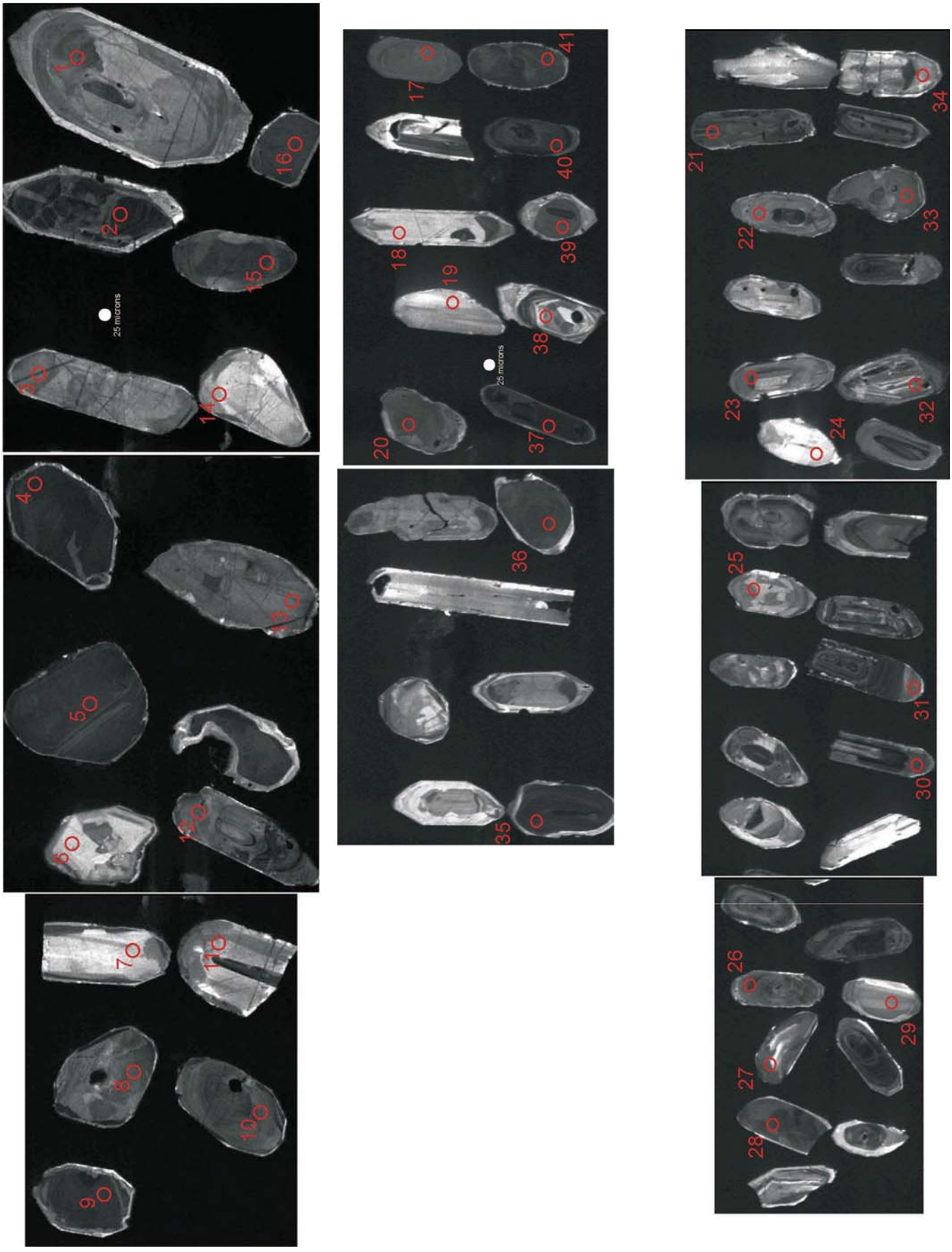

Figure 1. Cathodoluminescence images of representative zircon crystals extracted from granodiorite. Taken March 23, 2015.

Table 2. LA-ICP-MS U-Pb age summary.

Sample*	Lithology	U-Pb age Ma**	MSWD†	Probability of Fit	*N*
KCS-13-44	Rhyolite ash flow tuff	77.4 ± 0.8(1.7)	1.6	0.002	69
KCS-13-28	Rhyolite ash flow tuff	78.5 ± 1.6(2.2)	2.1	0.003	21
KCS-13-12	Diorite	79.8 ± 1.1(1.9)	2.0	0.001	31
E-25	Granodiorite	1,777.00 ± 8(20)	3.8	0.000	41

*Sample locations: KCS-13-44 (46.28289, -112.52848), KCS-13-28 (46.35218, -112.52848), KCS-13-12 (46.28729, -112.59713), E-25 (46.2308, -112.3431).
**Ages are inverse-variance weighted mean $^{206}Pb/^{238}U$ ages, except for sample E-25, which is reported as the $^{207}Pb/^{206}Pb$ age; uncertainties are reported as X(Y), where X = internal error (95% confidence interval including geological scatter), and Y = external error including standard calibration uncertainty (1% for $^{207}Pb/^{206}Pb$ and 2% for $^{206}Pb/^{238}U$, 2-sigma).
†MSWD, mean squared weighted deviation.

STRUCTURE

The volcanic rocks of the Emery mining district were subject to regional compressive deformation during the Laramide orogeny that lasted approximately 75 to 55 Ma (Houston and Dilles, 2013). Thrust faulting took place in an eastward direction during regional compressive deformation. Laramide compression evolved into an extensional event, which resulted in a period of normal faulting. This period of normal faulting is suggested to be synchronous with the eruption of the 53 to 48 Ma Lowland Creek Volcanics (Houston and Dilles, 2013).

After thrust faulting occurred, there was a period of bedding plane and normal faulting. The earlier bedding plane and normal faults in the district are occupied by polymetallic veins. Later normal faulting structures are un-mineralized, cutting and offsetting the mineralized veins. The mineralized veins are hosted by two sets of faults trending north–south and east–west. A major north–south-trending vein, approximately 1.5 km or 0.9 mi in length, extending from the Argus mine in the north to the Bonanza mine in the south, was mapped by Derkey (1986; also plate 1). This vein has a variable shallow dip ranging from 5° to 40° to the east and follows the amygdaloidal zones in the basalt–andesite flows. In steeper dipping sections, the vein cuts the amygdaloidal zones and volcanic flows. Robertson (1953) describes these shallow dipping mineralized faults as bedding plane faults or low-angle reverse faults. These faults most likely formed in planes of weakness in the volcanic rocks during the final episode of Laramide compression.

A number of east–west-striking normal faults hosting the veins were mapped by Derkey (1986; also plate 1). These faults are perpendicular to the major north–south reverse fault cutting across the district, have 80° to vertical dips, and can reach up to 1.5 km (0.9 mi) in length. Development of these normal faults took place prior to the mineralizing event and could be related to the development of the north–south reverse fault. These normal faults are described by Derkey (1986) to be tear faults that developed during the thrusting event that developed the north–south reverse fault. They may have developed during a Laramide extensional event after the reverse faulting event. Veins occupying the normal faults are just as mineralized as veins occupying the reverse fault; Robertson (1953) reported these veins to have a high gold and silver content.

Later, non-mineralized normal faults offset the older mineralized faults (Derkey, 1986) and occur throughout the district (plate 1). There are two sets of faults: earlier developed, northeasterly trending structures and later, northwesterly trending faults. The older, northeasterly trending fractures do not offset the veins to any extent and are described as tight shears by Robertson (1953). Later, northwesterly trending, post-mineralization faults have large displacements offsetting some of the veins. The Black Rock fault, in the southern part of the district, is described by Robertson (1953) as having from N. 70° to 75° W. strike and displaces the Emery vein on a horizontal plane by 500–1,000 ft, causing the south side of the vein to be offset to the west (plate 1). North of Baggs Creek on the north edge of the district is a fault that strikes N. 80° W. and offsets the westerly dipping basalt–andesite flows nearly 2,000 ft (Robertson, 1953). This fault has a surface expression that extends for 6.5 km (4 mi).

GEOPHYSICS

Investigations conducted by FMC from 1986 to 1989 indicated the volcanic rocks in the northern part of the district are domed into an asymmetric anticline. Brannon (1989) suggested that the doming was caused by intrusion of a laccolith under the volcanic rocks. Geophysical evidence published by the United States Geological Survey (USGS) consisting of a magnetic low suggests the presence of a deep-seated intrusion in this region. In 1994, the USGS published the results of a gravity and aeromagnetic survey for the Butte 1° x 2° quadrangle that included the Emery mining district. The aeromagnetic survey defined a magnetic low in the northern part of the district, north of Baggs Creek, and a magnetic low east of the district under Sugarloaf Mountain (plate 1). These magnetic lows are interpreted by Hanna and others (1994) to be strongly altered intrusions. A similar magnetic low is present under the Butte district and is interpreted to be pervasive alteration of the Butte granite (Hanna and others, 1994). A gravity high extending into the district is interpreted to be related to the Elkhorn Mountains Volcanics (Hanna and others, 1994).

WALL-ROCK ALTERATION

Alteration of the volcanic rocks is widespread throughout the Emery mining district and took place during vein development. The alteration types parallel and grade outward from the veins. Silicic and carbonate alteration is found adjacent to the veins and grades outward to sericitic alteration, which grades into argillic alteration. Propylitic alteration is found the farthest from the veins, and most volcanic rocks in the district are propylitically altered.

Eighteen samples of altered volcanic rocks were taken from 10 mining properties throughout the district. These samples were examined in thin section (fig. 2) to identify the various hydrothermal alteration types, history, and chemical changes. Zimmerman (2016) examined these samples using a PANalytical TerraSpec Halo mineral analyzer, identifying five types of alteration: propylitic, sericitic, argillic, carbonic, and silicic.

Propylitic Alteration

Propylitic alteration is widespread throughout the district and is characterized by the presence of Fe-Mg chlorite, Mg-illite, epidote, clinozoisite/zoisite, calcite, siderite, kaolinite, and pyrite (Zimmerman, 2016). Propylitic alteration was identified in the granodiorite intrusion and basalt–andesite that is most distal from the veins. In the granodiorite, biotite was replaced by chlorite, with minor hydrothermal muscovite (sericite) replacing plagioclase along fractures and on crystal margins. In the basalt–andesite, original crystal shapes are preserved consisting of pyroxene and plagioclase phenocrysts and plagioclase laths in the groundmass (fig. 2A). Plagioclase was altered to Mg-illite, calcite, and quartz while pyroxenes were altered to Fe-Mg chlorite, epidote, clinozoisite/zoisite, and pyrite. Ferrihydrite and vermiculite are recent weathering products that can be present in propylitically altered basalt–andesite.

Sericitic Alteration

Sericitic alteration is characterized by the presence of sericite, phengite, K-illite, quartz, and pyrite (Zimmerman, 2016). Sericitic alteration is found adjacent to the veins and envelops silicic alteration. The basalt–andesite groundmass is replaced by fine-grained quartz and muscovite, with plagioclase and pyroxene being replaced by muscovite and K-illite (fig. 2B). Excess iron was incorporated into subhedral to euhedral pyrite cubes and pyritohedron. The granodiorite intrusion was likewise highly altered by sericitic alteration.

Argillic Alteration

Argillic alteration is present throughout most of the volcanic rocks in the district. Argillic alteration is characterized by K-illite, montmorillonite, sepiolite (identified by TeraSpec analysis), and quartz (Zimmerman, 2016). The groundmass is replaced by K-illite and quartz intergrowths and patches of dolomite and ankerite (figs. 2E, 2F). The presence of carbonate alteration suggests argillic and carbonate alteration overlap in time and space. Argillic alteration was subject to recent weathering, indicated by pyrite and Fe-bearing minerals being replaced by goethite and ferrihydrite.

Carbonic Alteration

This stage is characterized by the carbonate minerals: ankerite, calcite, dolomite, kutnohorite, and rhodochrosite. These were identified by X-ray diffraction analysis and SEM EDS at the Center for Advanced Metallurgical Processing (CAMP), Montana Tech. Carbonate minerals replace volcanic wall rock; the most common minerals are ankerite, calcite, and high iron dolomite (fig. 2C). These carbonate minerals fill fractures and open spaces in brecciated volcanic wall rocks and completely to partially replace breccia frag-

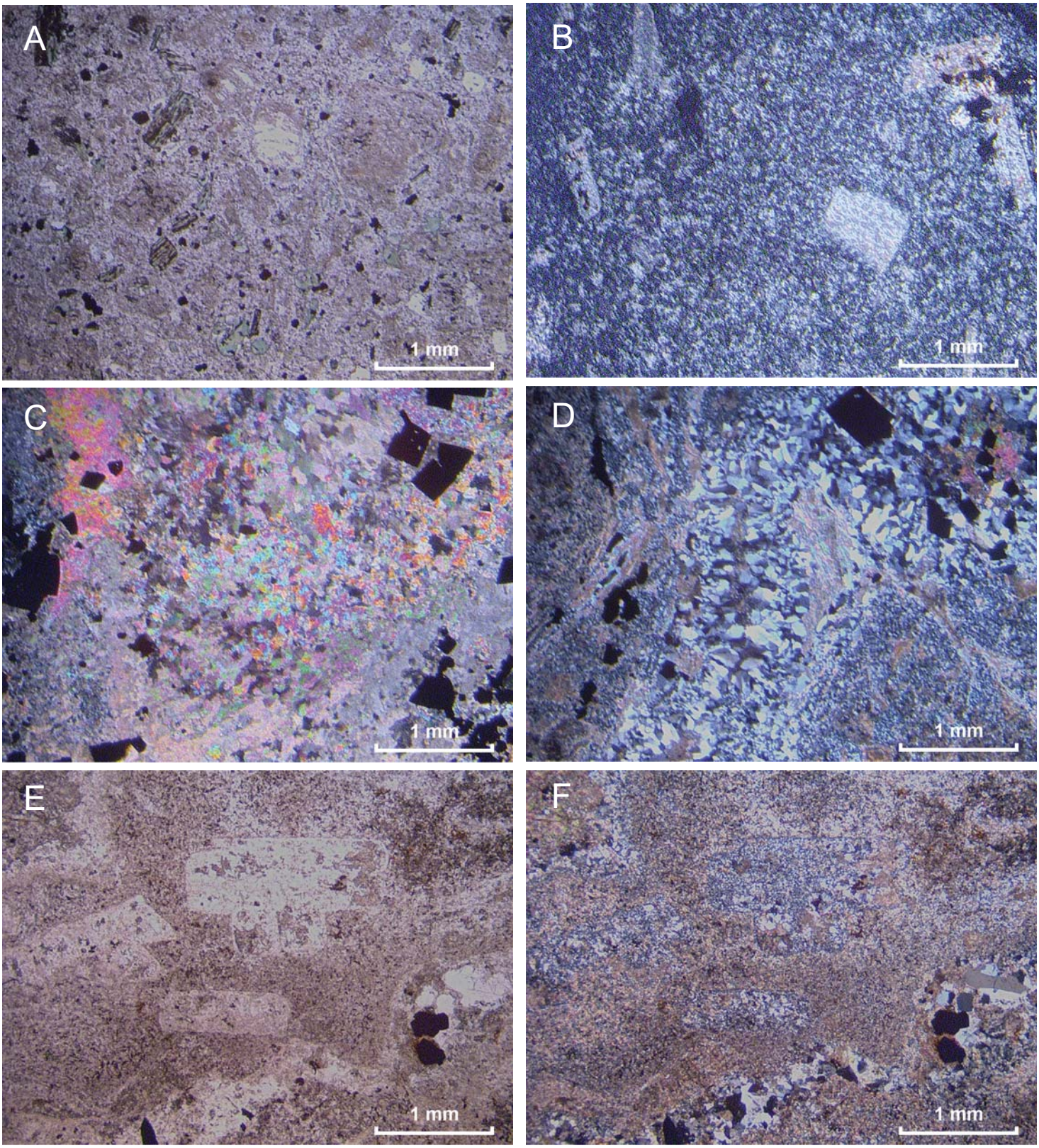

Figure 2. Alteration types in thin section. (A) Propylitically altered basalt–andesite. Plagioclase and pyroxene altered to chlorite with quartz, illite, and siderite matrix. Image in plane polarized light (PPL). (B) Sericitic alteration, plagioclase, and groundmass altered to sericite and fine-grained quartz. Image in crossed polarized light (XPL). (C) Carbonic alteration in XPL, groundmass altered to carbonate and iron minerals replaced by pyrite. (D) Silicic alteration in XPL, groundmass replaced by fine-grained quartz, coarse-grained quartz filling open spaces and minor replaced carbonate remaining. (E) Argillic alteration in PPL, showing remains of altered plagioclase. (F) Argillic alteration in XPL with plagioclase altered to sericite and groundmass altered to clays, quartz, and carbonate.

ments. Plagioclase and pyroxene in the groundmass are replaced by carbonate minerals. Zimmerman (2016) identified two clay minerals, palygorskite and beidellite, from TerrSpec Halo analysis. Palygorskite is an alteration product of Mg-silicates, and beidellite is an Al-rich variety of montmorillonite. These minerals may represent the alteration of Mg-illite and chlorite, and occur along the rims of breccia clasts (Zimmerman, 2016).

Silicic Alteration

Silicic alteration is recognized as wall-rock replacement by quartz and microcrystalline silica and is found on the vein margins. Brecciation and fracturing took place in the wall rock adjacent to the veins opening channel ways for hydrothermal fluid invasion. These fractures are filled with coarse-grained quartz and they cut earlier dolomite veins (fig. 2D). Breccia fragments are partially to totally replaced by quartz leaving a gray, fine-grained, quartz groundmass. Quartz veins show replacement along contacts with early dolomite veins. Some quartz veins have minor sericite inclusions and sericite occurs along the margins. Coarse-grained quartz fills open spaces. Fine-grained quartz partially to completely replaces the carbonate groundmass and sericite. Silicic alteration grades outward from the veins into sericitic alteration (Stejer, 1948).

ALTERATION LITHOGEOCHEMISTRY

Each alteration type was analyzed by whole-rock methods from 16 samples. Whole-rock analysis was performed by ALS Minerals Laboratory. ALS code ME-ICP06 procedure was applied, which uses a lithium borate fusion followed by acid digestion and inductively coupled plasma-atomic emission spectrometry (ICP-AES) finish. Element oxide results are reported in weight percent and are shown in appendix B.

To delineate the lithogeochemistry, the Ishikawa alteration index (AI) and chlorite–carbonate–pyrite index (CCPI) were determined for each alteration type. The AI defines the intensity of sericite and chlorite alteration and the ratios principal rock-forming elements gained during sericite and chlorite alteration ($MgO + K_2O$) over the elements lost and gained ($Na_2O + CaO + MgO + K_2O$) (Large and others, 2001). For hydrothermally altered rocks, the AI is between 50 and 100, with 100 representing a complete replacement of feldspars by sericite and/or chlorite (Large and others, 2001). Because silicic and carbonic altered rocks do not have an abundance of sericite or chlorite, they would have an AI below 50 but are still hydrothermally altered. The CCPI measures the degree of chlorite alteration by measuring the increase in MgO and FeO and the loss of Na_2O and K_2O from replacement of albite, K-feldspar, and sericite (Large and others, 2001). Large and others (2001) also determined the CCPI is positively affected by Mg-Fe carbonate alteration and pyrite, magnetite, or hematite enrichment. The CCPI is strongly affected by magmatic fractionation and primary composition variations of volcanic rocks (Large and others, 2001), which can result in different values for granodiorite and basalt–andesite.

The values and corresponding alteration types for the AI and CCPI are shown in table 3 and are plotted on an alteration box diagram (fig. 3). By plotting the AI and CCPI against each other, different alteration types cluster in distinctive fields on the box diagram, reflecting a unique lithogeochemistry. For example, silicic alteration lacks sericite and carbonate, has the lowest AI (36.6) and CCPI (31.6), and plots in the lower left field on the box diagram. In contrast, sericitic alteration, which has a variable chlorite–pyrite content, has the highest AI (83.3 average) with a variable CCPI (43.1–75.7), and plots in a field on the right side of the diagram between 100% sericite and 100% chlorite–pyrite alteration. Carbonate alteration has the highest average CCPI (80.15) but a low average AI (40.4) and plots in a field near the top of the diagram, approaching complete dolomite and ankerite alteration. Argillic alteration, which lacks sericite but has variable carbonate, pyrite, and chlorite, has a lower average AI (54.4) and elevated average CCPI (72.8) and plots in a field near the top-central part of the diagram. Of all the alteration types (with the exception of silicic), propylitic alteration has the lowest average AI (42.7) and a variable CCPI, plotting near the center of the diagram. The variable CCPI (54.0–5.8) is a reflection of the variable carbonate, chlorite, and pyrite composition found in propylitic alteration. The variable compositions of argillic and propylitic alteration cause the two fields to partially overlap. Because propylitic alteration and amygdaloidal basalt–andesite could have a high concentration of carbonate minerals, they will have a high CCPI nearing the carbonic field.

Oxide averages that show the most variation due to alteration (MgO, Fe_2O_3, Na_2O, K_2O, CaO, and SiO_2) are plotted against each alteration type (fig. 4). The plots show unique variations in oxide composition for each alteration type. Each alteration type is also plotted against the average AI and CCPI and likewise demonstrate unique variations (fig. 4).

Silicic alteration shows the most depletion in

Table 3. Alteration index (AI) and chlorite-carbonate-pyrite index (CCPI) values and corresponding alteration, rock types, and sample numbers.

Sample Number	Rock Type	Alteration Type	AI	CCPI
E-3	Basalt andesite	Carbonic	42.4	78.8
E-7	Basalt andesite	Sericitic	72.6	75.7
E-25	Granodiorite	Propylitic	45.0	54.0
E-26	Granodiorite	Sericitic	96.0	49.6
E-38	Basalt andesite	Argillic	51.8	75.3
E-43	Basalt andesite	Sericitic	78.0	43.1
E-48	Basalt andesite	Sericitic	92.7	75.5
E-63	Basalt andesite	Argillic	53.2	70.9
E-65	Basalt andesite	Carbonic	43.6	83.1
E-66	Basalt andesite	Silicic	36.6	31.6
E-67	Basalt andesite	Sericitic	77.0	71.6
E-68	Basalt andesite	Argillic	50.5	71.6
E-69	Basalt andesite	Argillic	55.7	72.9
KCS-13-18	Basalt andesite	Argillic	61.0	73.5
KCS-13-22	Basalt andesite	Propylitic	45.6	68.6
KCS-13-24	Basalt andesite	Propylitic	53.0	56.6
R-1	Basalt andesite	Carbonic	36.5	78.0
R-2	Amygdaloidal basalt	Propylitic	36.7	71.0
R-3	Basalt andesite	Carbonic	39.0	80.7
R-4	Basalt andesite	Propylitic	30.0	59.6
R-5	Basalt andesite	Propylitic	45.6	75.8

Note. For sample numbers R-1 to R-5, AI and CCPI were calculated using whole-rock analysis from Robertson (1953).

CaO, K_2O, MgO, and Fe_2O_3 of all the alteration types, caused by the replacement of the original host rock by quartz (fig. 4). Silicic alteration has the highest Na_2O wt% of all the alteration types, caused by albitization. Silicic alteration also has the lowest AI and CCPI, reflecting the lack of sericite, carbonate, chlorite, and pyrite (fig. 4).

In contrast to silicic alteration, carbonate alteration shows a depletion in Na_2O and SiO_2, with little change in K_2O and an enrichment in CaO, MgO, and Fe_2O_3 caused by the development of carbonate minerals replacing plagioclase and pyroxene. Carbonate alteration has the highest average CCPI compared to the other alteration types and a slight increase in the AI compared to silicic alteration.

Sericitic alteration has the highest enrichment of K_2O compared to the other alteration types and highest AI, caused by sericite replacing feldspars, micas, and pyroxenes of the original basalt–andesite (fig. 4). Sericitic alteration is characterized by the depletion of MgO, CaO, and Na_2O, and an enrichment in SiO_2. There is a slight depletion in Fe_2O_3 between sericitic and carbonic alteration. The average CCPI is lower than carbonate and argillic alteration due to the lack of chlorite, carbonate, and pyrite in sericitic alteration.

Argillic alteration has the highest average MgO wt% of all the alteration types and the second highest average CCPI, caused by the generation of magnesium-enriched clays montmorillonite and sepiolite and the presence of pyrite (fig. 4). Compared to sericitic alteration, argillic alteration shows a minor change in K_2O being slightly decreased, reflecting the generation of K-illite from the replacement of orthoclase. The generation of montmorillonite is reflected in the increase in CaO and Na_2O compared to sericitic alteration. The Fe_2O_3 wt% is similar to sericite, with a slight decrease from the replacement of pyroxene minerals and primary magnetite. Compared to sericitic alteration, there is a decrease

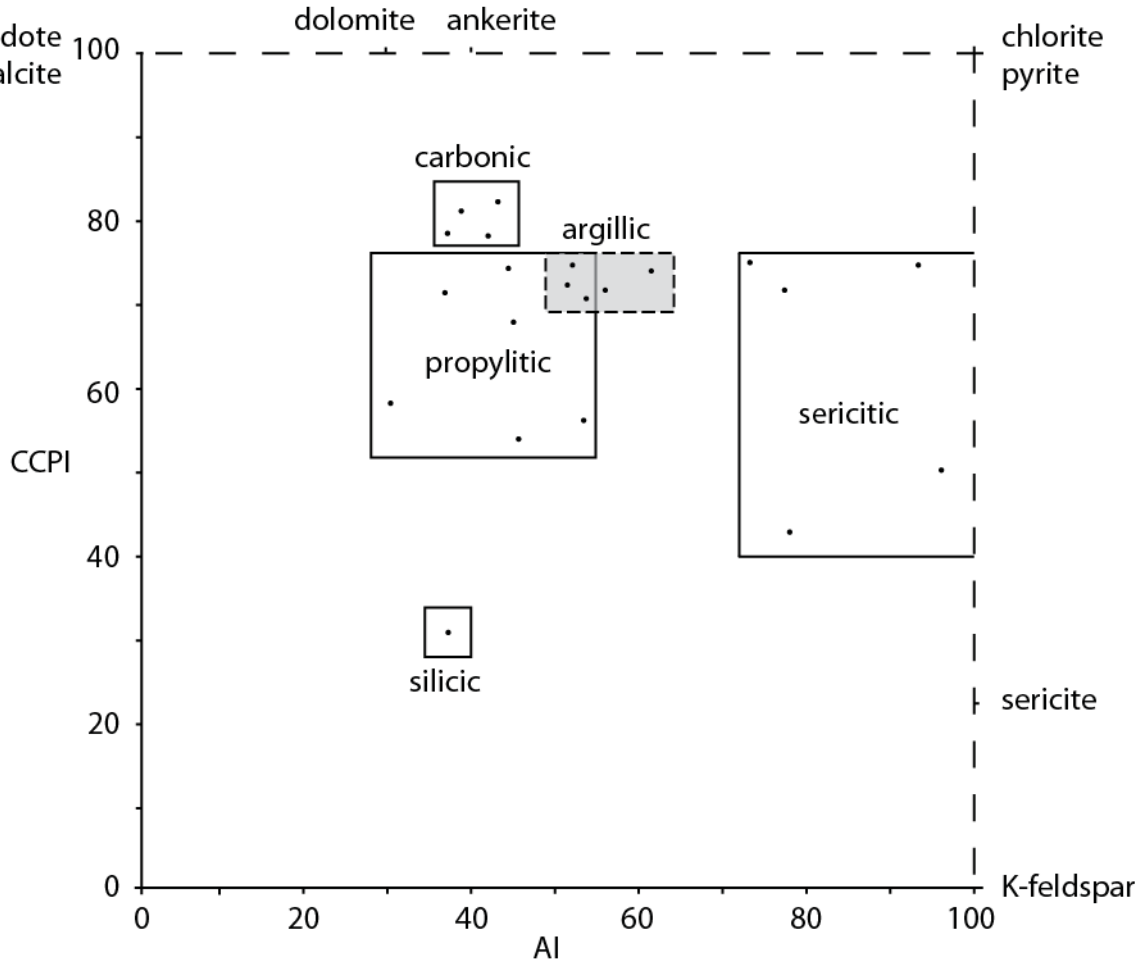

Figure 3. Alteration box diagram from Large and others (2001) showing fields for different alteration types. AI, Ishikawa alteration index. CCPI, chlorite—carbonate—pyrite alteration index.

in SiO_2, and compared to propylitic alteration, SiO_2 is similar. Because propylitic alteration partially overlaps argillic alteration (fig. 4), SiO_2, CaO, and Fe_2O_3 will have similar wt% values.

Propylitic alteration is enriched in Na_2O and Fe_2O_3, with CaO and K_2O being similar to argillic alteration and a depletion in MgO reflecting the generation of epidote, chlorite, clinozoisite-zoisite, Mg-illite, carbonate minerals, and pyrite (fig. 4). Compared to argillic alteration, propylitic alteration has a similar average K_2O wt% caused by illite generation. Because propylitic alteration contains little sericite, it will have a low AI but will have an elevated CCPI on account of the presence of chlorite, carbonates, and pyrite. The CCPI and AI is variable (fig. 4) because of variations in chlorite, carbonate, and pyrite concentrations and different degrees of alteration.

VEIN MINERALOGY

Twenty-three polished sections and 14 thin sections examined for this study confirmed some of the findings of early investigations, and new data were added to the known mineralogy. SEM-backscatter emission (BSE) for polished sections from the Emery mine are shown in figure 5 (from Zimmerman, 2016). This study was not confined to one mine but covered all the known mines and veins throughout the district. Minerals identified from this study and those reported by past investigations are reported in table 4.

Sulfides and Sulfosalts

Sulfides and sulfosalts are the most economically important vein minerals listed in table 4. Ten of these minerals were identified from polished sections and polished thin sections using reflected light and transmitted light microscopy, and scanning electron microscope-energy dispersive spectrum (SEM-EDS) techniques. The SEM-EDS analysis was performed at CAMP. Minerals were also identified from examinations of hand specimens. Two previously identified sulfide minerals not found in this study are molybdenite, reported by Freeport-McMoRan from three drill holes (Brannon, 1989), and millerite, reported by Robertson (1953) from the Argus Mine.

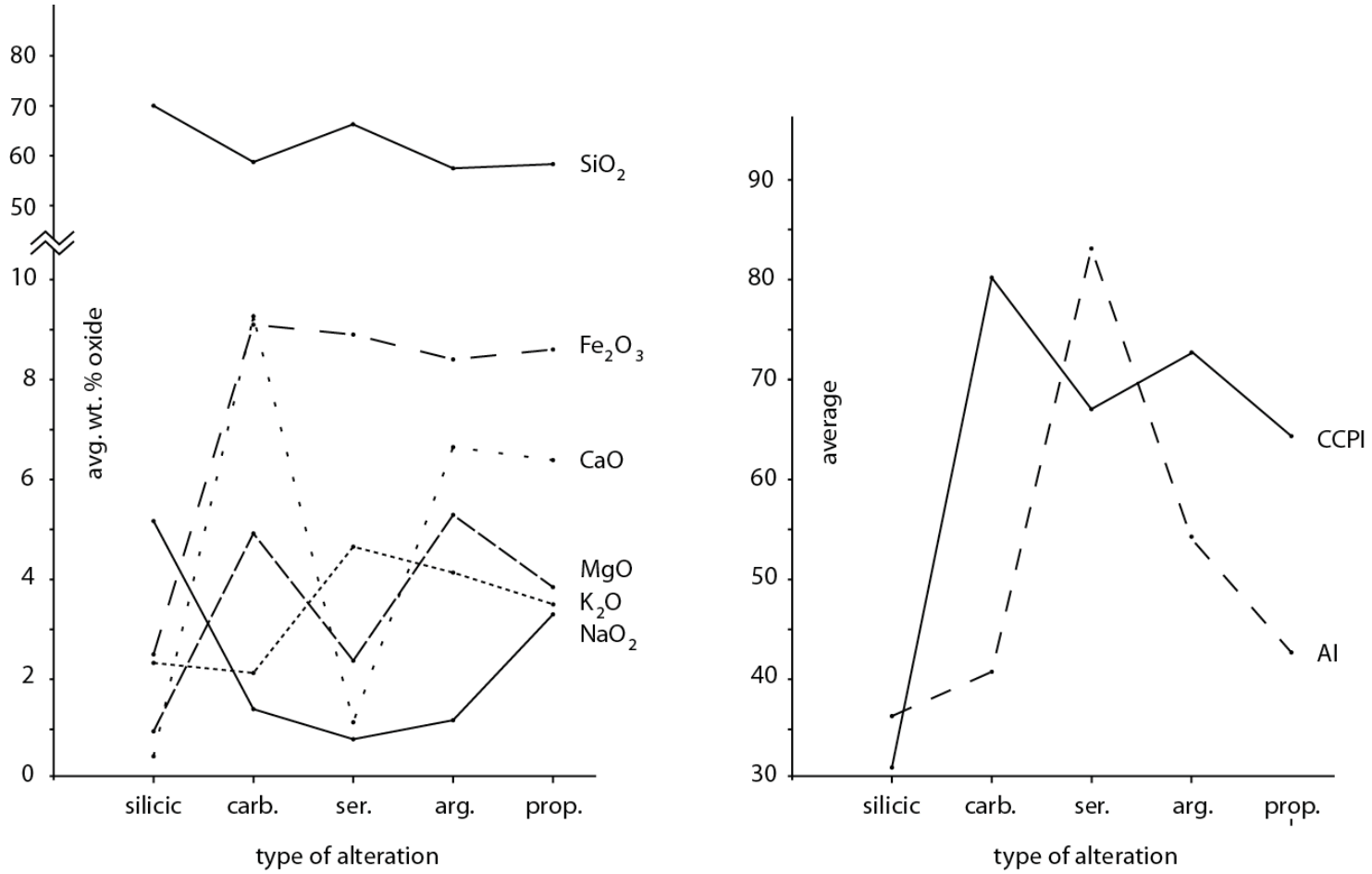

Figure 4. Plot of alteration types showing depletions and enrichments of oxide averages and changes in alteration index (AI) and chlorite–carbonate–pyrite alteration index (CCPI) with respect to alteration types.

Native Element

Electrum, a gold–silver solid solution, is the only occurrence of native metal identified during this investigation. Elliott (1939) reported on a gold particle he etched from an ankerite vein collected from the Emery mine. Electrum was identified here in a polished section using SEM-EDS techniques, which yielded Au/Au+Ag = 0.62 wt%—a high silver content. In SEM-backscatter images, electrum was observed as rounded grains included in freibergite. A rounded electrum grain was observed to occur in the contact between Ag-rich tetrahedrite and sphalerite (fig. 5B).

Quartz

Quartz is a common gangue mineral found in all the veins and altered rocks. Vein quartz fills open spaces and is found as comb, massive, zoned structures and colloform. Zoning in quartz consists of alternating layers of milky to clear gray crystals. Colloform quartz was initially an amorphous gel that recrystallized (Dong and others, 1995). Quartz is present in every paragenetic stage and can be delineated by fluid inclusion and sulfide assemblages. Stage 2 quartz has type 1 and type 2 and CO_2-enriched fluid inclusion assemblages and is associated with arsenopyrite and pyrite, while stage 3 quartz is associated with Pb-sulfide/sulfosalts and has type 1 fluid inclusions. Late-stage quartz is associated with late-stage carbonate mineralization.

Carbonates

Carbonate minerals are found throughout the veins and altered host rocks. Four carbonate minerals reported by past investigators identified these minerals from thin sections, microchemical tests, and physical properties. Carbonate minerals were identified using SEM-EDS and X-ray diffraction (XRD) analysis at CAMP. Ankerite is the most common carbonate mineral and is intergrown with dolomite occurring as patches in the carbonate replacement stage. Fine-grained sulfides are disseminated in dolomite (figs. 5C, 5D). Calcite was one of the last hypogene minerals to be deposited and occurs in the matrix of carbonate breccia and late-stage, cross-cutting carbonate veins. Kutnohorite and rhodochrosite were deposited during early vein development and continued with the precipitation of arsenopyrite and pyrite.

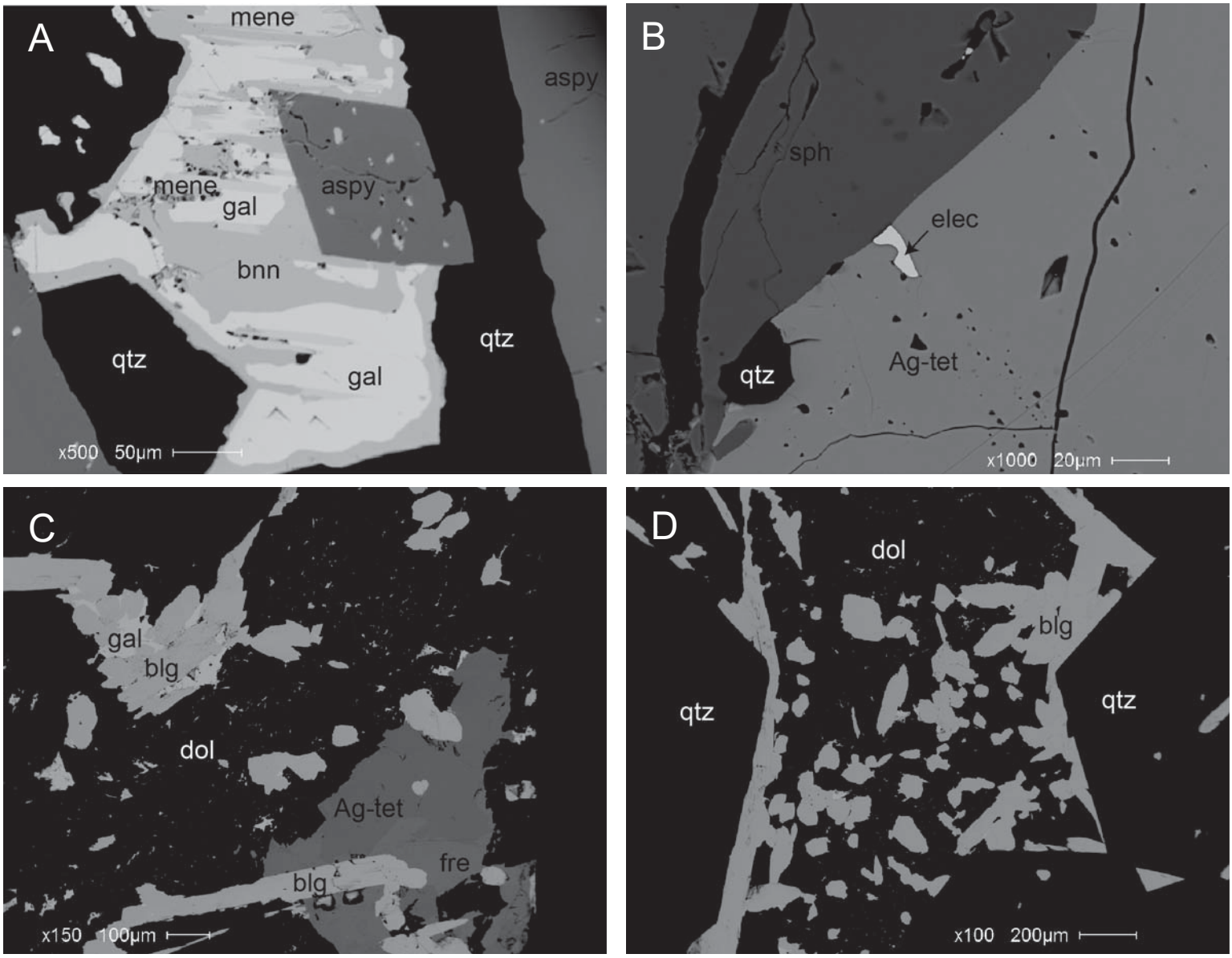

Figure 5. SEM-BSE images of ore minerals from the Emery mine. (A) Euhedral arsenopyrite (aspy) partially enclosed by galena (gal), meneghinite (mene), and bournonite (bnn) in quartz (qtz) matrix. Gal is partially replaced by bnn and mene. (B) Rounded electrum (elec) grain included in Ag-rich tetrahedrite (Ag-tet) along sphalerite (sph) grain margin. (C) Anhedral grain of gal and associated boulangerite (blg) in a dolomite (dol) matrix. Anhedral Ag-tet grain partially enclosing freibergite (fre) grain, subhedral blg grain partially enclosed by Ag-tet and fre. (D) Anhedral to euhedral blg grains in a dol matrix filling open space between qtz crystals. Rounded blg grains showing dissolution.

Table 4. Minerals identified from the Emery veins by SEM-EDS, X-ray diffraction, and reflected and transmitted light microscopy.

Sulfides and Sulfosalts	
Arsenopyrite	FeAsS
Boulangerite	$Pb_5Sb_4S_{11}$
Bournonite	$PbCuSbS_3$
Chalcopyrite	$CuFeS_2$
Freibergite	$Ag_6Cu_4(Fe,Zn)_2Sb_4S_{13}$
Galena	PbS
Meneghinite	$Pb_{13}CuSb_7S_{24}$
Millerite	NiS
Molybdenite	MoS_2
Pyrite	FeS_2
Pyrrhotite	$Fe_{1-x}S$ x = 0.1–0.2
Sphalerite	ZnS
Tetrahedrite	$Cu_6Cu_4(Fe,Zn)_2(Sb,As)_4S_{13}$
Native Element	
Gold variety electrum	X Au:Ag = 0.62 wt%
Silicate	
Quartz	SiO_2
Carbonate Minerals	
Ankerite	$Ca(Fe^{2+},Mg,Mn)(CO_3)_2$
Calcite	$CaCO_3$
Dolomite	$CaMg(CO_3)_2$
Kutnohorite	$Ca(Mn,Mg)(CO_3)_2$
Rhodochrosite	$Mn^{2+}CO_3$

Note: Molybdenite and millerite reported by past investigators but not identified during this investigation.

VEIN PARAGENESIS

Using data presented from past investigations by Derkey (1986) and Al-Khirbash (1982) with new observations, we ascertained a reinterpreted paragenetic sequence (fig. 6) that includes four mineralizing stages. These four stages were determined from polished and thin section petrography, electron microprobe analysis (EMPA), SEM-EDX, and XRD. EMPA was performed at Washington State University's GeoAnalytical Lab (Zimmerman, 2016). The vein mineralogy was found to be similar to that reported in previous investigations.

Stage 1

Stage 1 is dominated by carbonate and quartz mineralization and began with the introduction of CO_2-rich fluids. Quartz, dolomite, calcite, and ankerite replaces plagioclase and fills fractures in the basalt–andesite host rock along with minor disseminated pyrite. Near the close of stage 1, minor sulfidation of mafic minerals occurred, resulting in the formation of disseminated pyrite. Many of the early carbonate minerals were replaced during development of stages 2 and 3, making the original mineralogy difficult to interpret.

Stage 2

The second mineralizing stage was the beginning of metal deposition and is characterized by carbonate minerals, quartz, pyrrhotite, arsenopyrite, and pyrite. Carbonate mineralization was followed by silicification, causing the partial replacement of carbonate minerals with quartz (fig. 2D). During silicification, quartz-filled fractures developed, cross-cutting earlier carbonate minerals; pyrrhotite, arsenopyrite and pyrite were being crystallized. Pyrrhotite is found as inclusions in pyrite and most likely formed under early high-temperature and low-sulfur fugacity conditions needed for stabilization. Arsenopyrite can contain submicrometer gold particles identified by EMPA; fire assays by Elliott (1939) confirm the EMPA results (Zimmerman, 2016). Textures show open-space filling by euhedral comb quartz and euhedral arsenopyrite. Additional carbonate minerals and quartz were deposited near the close of this stage, enclosing arsenopyrite crystals in vugs and fractures.

Stage 3

Most of the base metals and silver were deposited during the third mineralizing stage. This stage is characterized by quartz, carbonate, sulfide and sulfosalt minerals, and electrum. All of the minerals

are intergrown, replacing, or included in others, making it difficult to determine the mineralizing sequence (fig. 5). The beginning of the third mineralizing stage (fig. 6) overlaps the second stage, with sphalerite and galena enclosing arsenopyrite and early stage pyrite. When sphalerite and pyrite were being deposited, boulangerite and galena started crystallizing simultaneously, overlapping and intergrowing with sphalerite and pyrite. At the same time, minor dolomite and ankerite were introduced, replacing boulangerite along grain margins and filling open spaces (figs. 5C, 5D). Galena and boulangerite were partially replaced on grain margins by later crystallized sphalerite. Chalcopyrite fills open spaces and partially replaces sphalerite on grain margins and is included in sphalerite along cleavage planes. The placement of bournonite and meneghinite in the paragenetic sequence is difficult because these minerals were only found in one polished section. Bournonite and meneghinite replace galena on grain boundaries, indicating development after galena, possibly late in the paragenetic sequence (fig. 5A). Sphalerite was the last sulfide mineral to crystallize during the third mineralizing stage.

Silver was introduced during stage 3 mineralization and three minerals formed: Ag-rich tetrahedrite, freibergite, and electrum (figs. 5B, 5C). Electrum

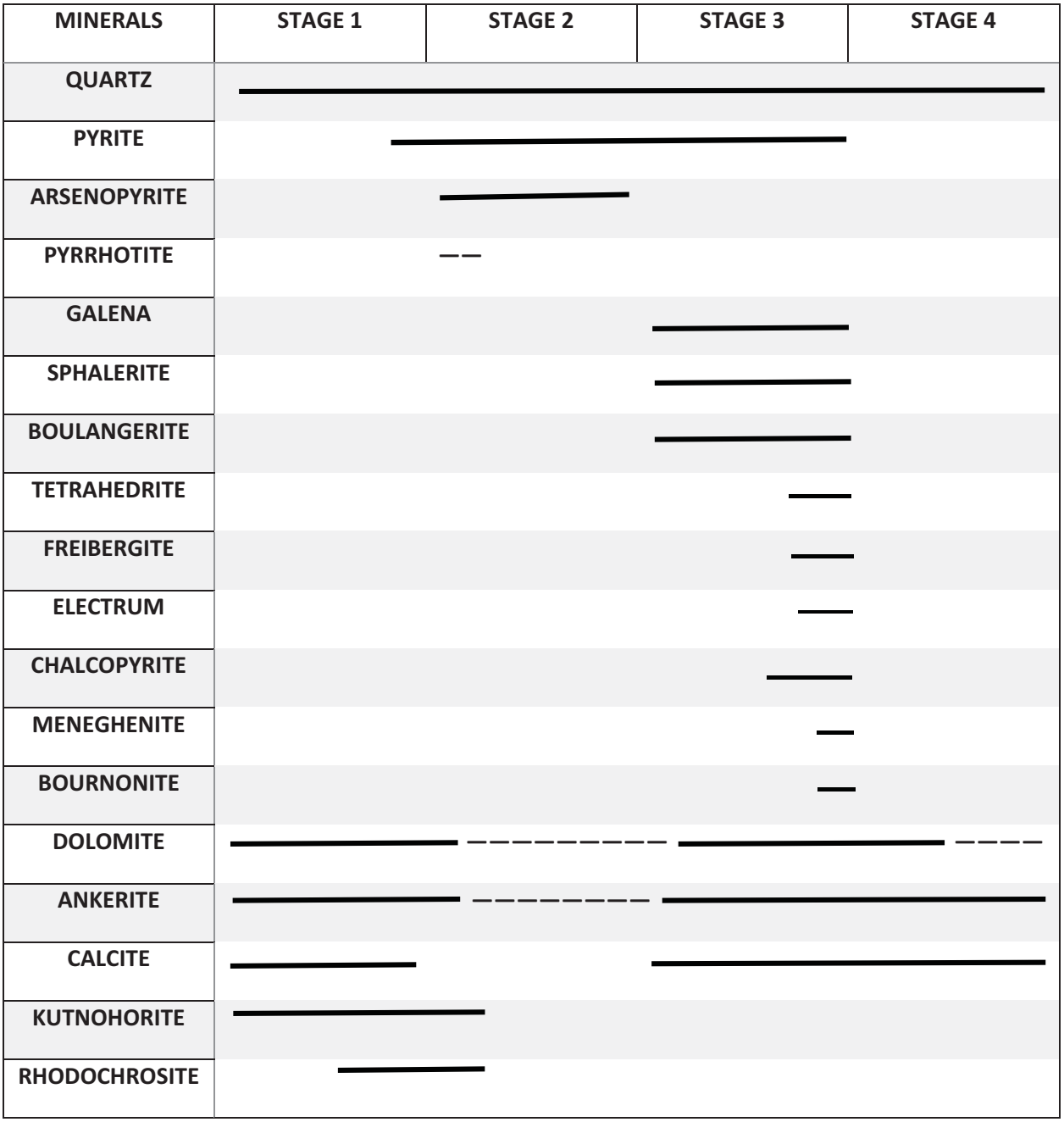

Figure 6. Vein paragenesis and mineralizing stages. Solid lines represent certainty and dashed lines represent relative uncertainty due to replacement textures.

occurs as rounded grains included in freibergite and along the margin between Ag-rich tetrahedrite and sphalerite. Tetrahedrite and freibergite are the principal silver-bearing minerals and crystallized in open spaces with other sulfide minerals. Both minerals can partially replace sphalerite on grain margins and most likely developed late in the paragenetic sequence.

Quartz occurs in a variety of forms, resulting from replacement of earlier crystallized phases and cyclic periods of brecciation and crystallization (fig. 7A). At the beginning of the third mineralizing stage, massive, white, fine to coarsely crystallized quartz filled open spaces in fault breccia along with sulfide minerals (fig. 7B). In addition, white, finely crystallized quartz replaced host rock breccia fragments within the faults. A second quartz generation fills fractures and open spaces in the earlier deposited quartz and sulfide minerals. Quartz from this second generation is milky to clear, coarsely crystallized, and forms comb structures in open spaces. This second quartz generation was later brecciated and fractured and a third quartz generation was deposited. This third quartz generation filled open spaces and fractures with clear, finely crystallized crusts.

Stage 4

The fourth stage is characterized by quartz and carbonate minerals: ankerite, calcite, and dolomite. Quartz is the most dominant mineral relative to carbonate. Quartz in stage 4 is in the form of chalcedony; clear, finely crystallized quartz occurs as crystal crusts lining open spaces as a final mineralizing event.

Hydrostatic pressures exceeding lithostatic pressure will cause the confining rocks to rupture and brecciate (Nelson and Giles, 1985; Burnham, 1985; Sillitoe, 1985). The developing veins experienced periods of hydrostatic over-pressuring, causing brecciation and microfracturing. Evidence for hydrostatic over-pressuring is shown in mineralizing stages 1–4 as microfractures and puzzle breccias (fig. 7).

FLUID INCLUSIONS

Fluid inclusions were selected from quartz samples collected from the Emery, Hidden Hand, Blue-Eyed Maggie, Paymaster, Elizabeth, and Argus mine dumps. Most of the inclusions analyzed came from low-angle veins with the exception of the Paymaster vein, which is a high-angle vein. The low-angle veins had the largest inclusions and populations of primary inclusions, while the high-angle veins had small, abundant inclusions and were not conducive to analysis. Microthermometry experiments were conducted by Zimmerman (2016) on a Fluid Inc.-adapted USGS gas-flow heating/freezing stage at the Geological Engineering Department, Montana Tech. Salinities were determined as wt% NaCl equivalent. MicroRaman spectroscopy was used to qualitatively identify the presence of CO_2 in the fluid inclusions (Zimmerman, 2016). Raman spectroscopic analysis was performed using a Renishaw in Via Raman Microscope at Montana Tech. Fluid inclusions were classified as primary or secondary using the textural classification by Roedder (1984).

Preliminary examination of 171 fluid inclusions showed a variety of inclusion types representing two distinct groups, aqueous and CO_2-rich, confirmed by laser MicroRaman (Zimmerman, 2016). Aqueous inclusions can be divided into type I and type II (figs. 8C, 8D). Type I inclusions contain a liquid-rich phase with a vapor bubble. Type II consist of a liquid and vapor phase, where the volume of the vapor phase exceeds that of the liquid phase. These two inclusion types are the most common, and are either primary or secondary, with the vapor phase homogenizing to brine. Daughter minerals are rare, but when present, are fibrous needles tentatively identified as dawsonite in carbon-dioxide-rich inclusions (fig. 8A). Zimmerman (2016) reported finding one type I inclusion with a halite daughter mineral and a type I inclusion with a dawsonite daughter mineral. Inclusions containing all vapor or liquid were also observed. Three phase fluid inclusions with liquid CO_2, water, and vapor and inclusions with liquid CO_2 and brine are present in some samples (fig. 8B). Secondary fluid inclusions consisting of two phase inclusions, all liquid and all vapor, occur along healed fractures. Groups of primary inclusions showing evidence of boiling occur as type I and type II along with all vapor and liquid inclusions.

Homogenization temperatures (Th) and wt% NaCl equivalent are summarized in table 5 and figure 9. The complete fluid inclusion dataset is shown in appendix C. Homogenization temperatures were determined for 138 fluid inclusions from the Emery, Hidden Hand, Paymaster, and Blue-Eyed Maggie mines. Primary type I and type II inclusions show no differences in Th for the different inclusion types. Fluid salinities using melting temperatures (Tm) of ice were determined from 80 inclusions. Melting temperatures of ice were determined by freezing and thawing, then recording Tm when the last ice crystal melted. From the Tm, fluid salinity was calculated using the methods by Roedder (1984) and are expressed as wt% NaCl equivalent.

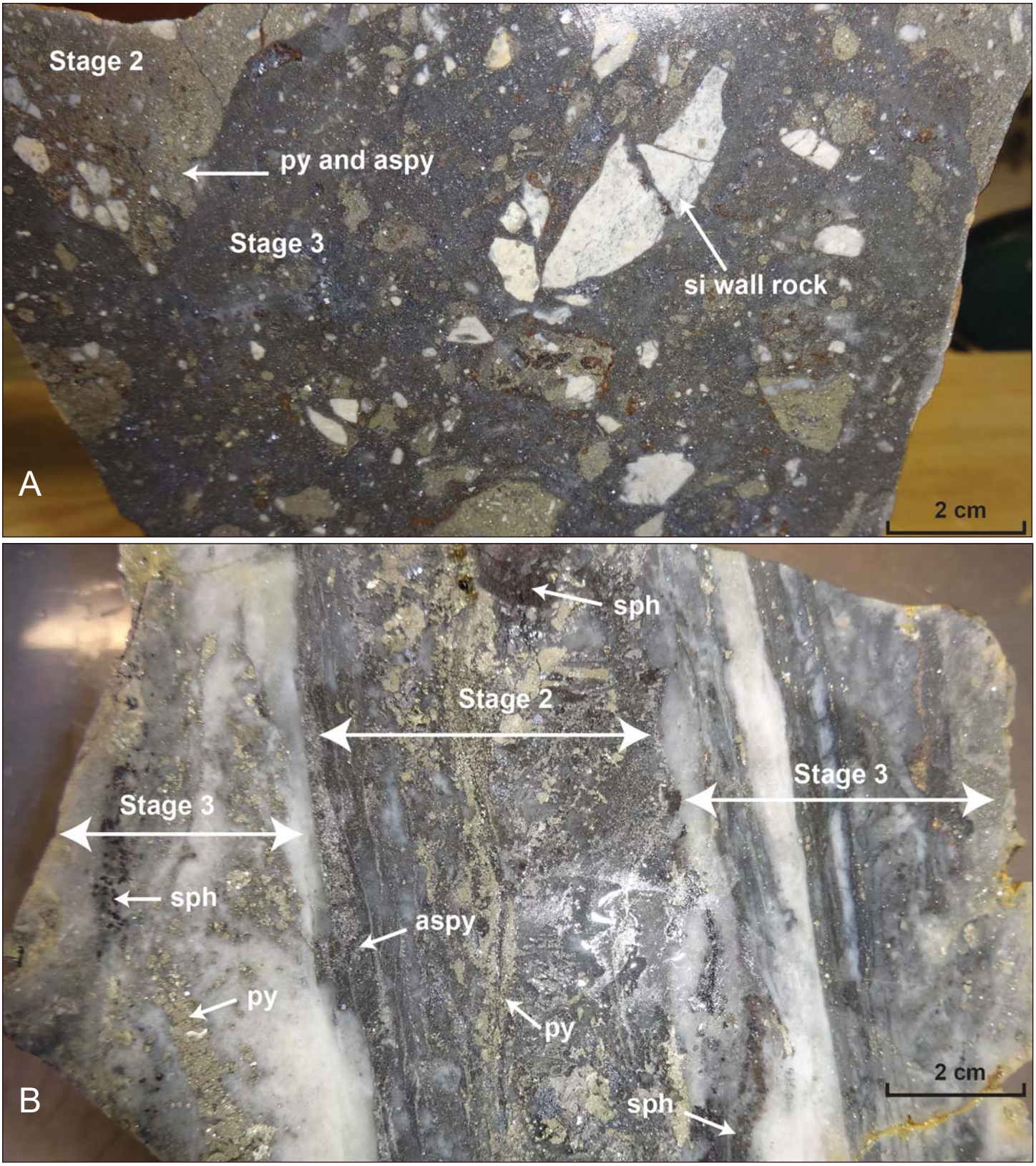

Figure 7. Photographs of cut slabs from vein sections. (A) Bonanza mine vein section showing two brecciation events. Basalt andesite wall rock was silicified (Si) and later brecciated. Stage 2 mineralization consisting of pyrite (py) and arsenopyrite (aspy) enclosing Si wall rock fragments was followed by a second brecciation event. Following the second brecciation event, stage 3 mineralization consisting of fine-grained galena, sphalerite, and gray quartz filling open spaces between the Si wall rock and stage 2 py breccia fragments. (B) Hidden Hand vein section showing mineralizing stages 2 and 3 and multiple quartz generations. Stage 2 mineralization with aspy, py, and dark to light gray quartz stringers and grains. Stage 3 mineralization consists of py and sphalerite (sph) with white quartz veins and brecciated stage 2 gray quartz with dark gray quartz stringers between breccia fragments.

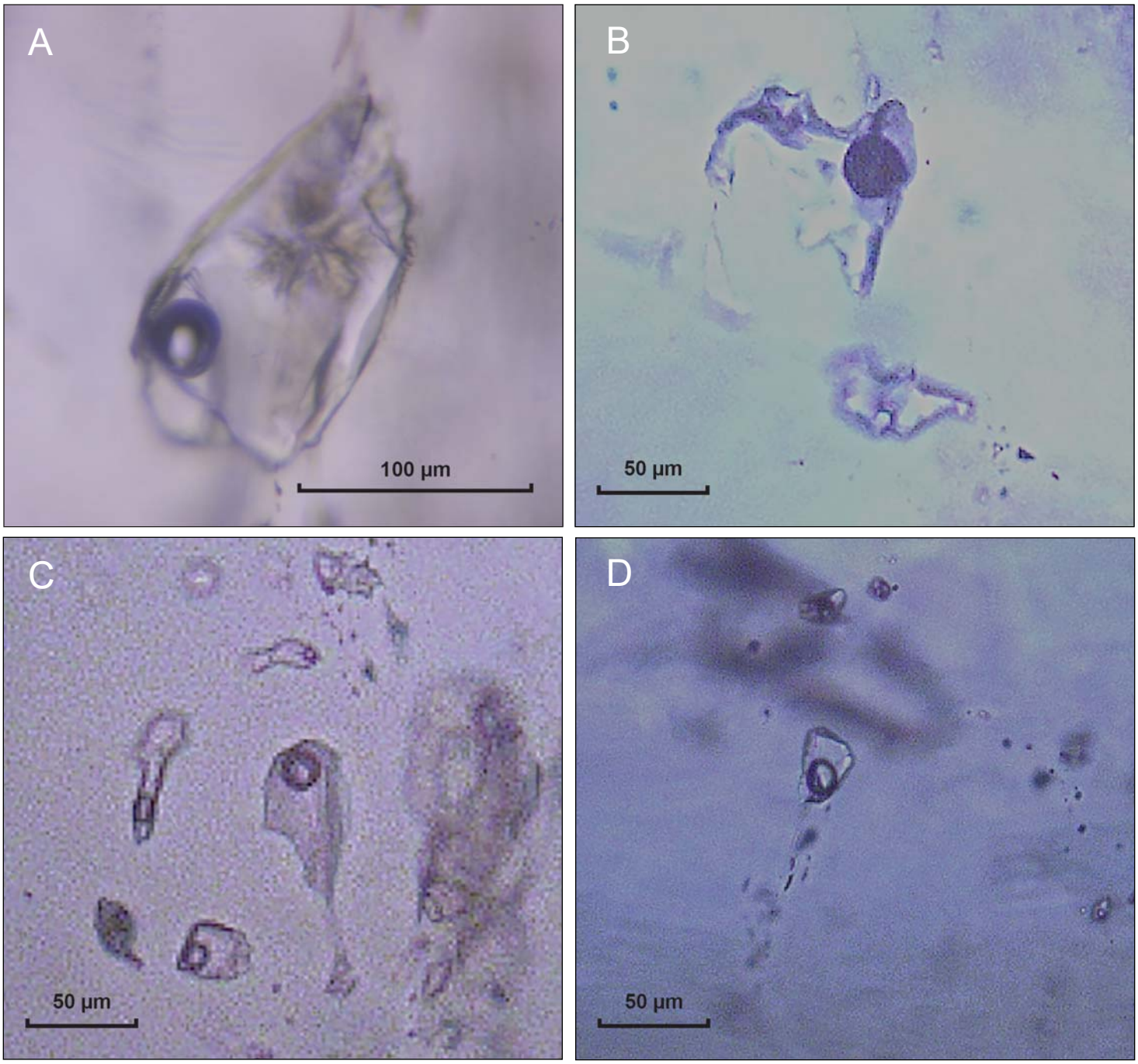

Figure 8. Photomicrographs of fluid inclusions. (A) Aqueous inclusion with CO_2 liquid and vapor bubble and dawsonite daughter mineral. (B) Liquid CO_2 bubble in aqueous inclusion. (C) Group of type I inclusions. (D) Type II inclusion.

Table 5. Summary of fluid inclusion data from 138 homogenization temperatures and corresponding 66 freezing point determinations from the Emery, Blue Eyed Maggie, Hidden Hand, and Paymaster mines.

Mineralizing Stage	ThºC Range	ThºC Average	Salinity Range	Salinity Average
2	282–354	310	0.0–8.8	5.8
3	223–278	260	5.3–7.7	6.3
4	127–219	218	0.6–7.9	5.5

Note. Complete data set shown in appendix C. ThºC temperature of homogenization in degrees centigrade. Salinity in wt% NaCl equivalent.

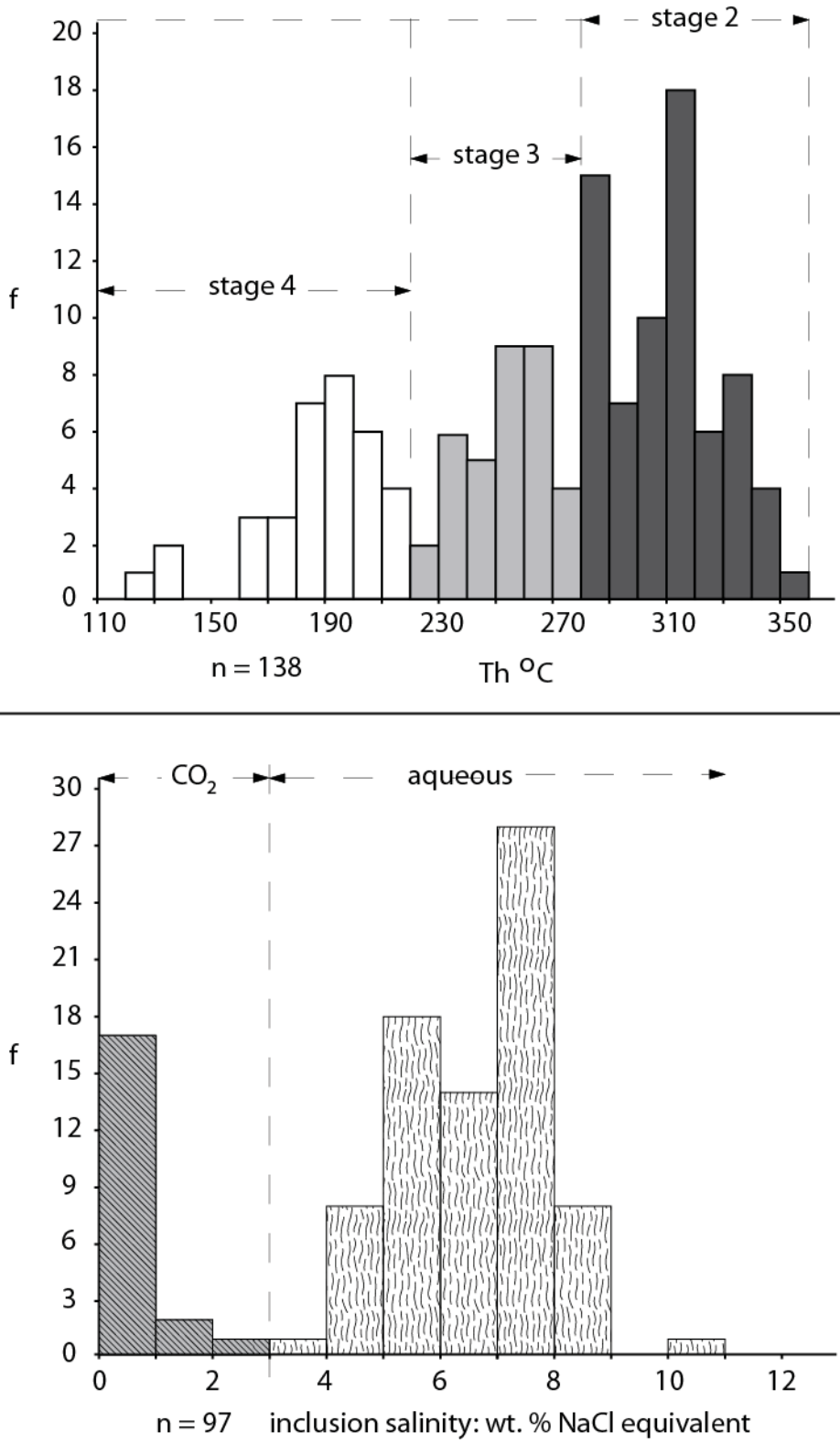

Figure 9. Cumulative frequency plots for fluid inclusion homogenization temperatures (Th°C) and salinity. Mineralizing stages 2–4 shown on homogenization temperature plot (top). Carbon dioxide (CO_2)-enriched fluid inclusions and aqueous inclusions with brine are shown on salinity plot (bottom).

The temperature cumulative frequency plot (fig. 9) shows three distinct fluid inclusion populations with peaks at 190°C, 260°C, and 310°C. The three populations represent mineralizing stages from the first sulfide stage to the final carbonate-quartz stage. Most sulfide mineralization took place during stages 2 and 3, which is where the highest Th was measured (table 5). Average salinities between the three stages show minor differences. For stage 2 the average Th is 310°C and average salinity is 5.8 wt% NaCl equivalent. Stage 3 mineralization represents a lower temperature with a Th of 260°C and an increase in salinity to an average 6.3 wt% NaCl equivalent. The final mineralizing stage has a decrease in temperature to an average Th of 218°C and a decrease in average salinity to 5.5 wt% NaCl equivalent. The average temperature changes between the mineralizing stages show decreasing temperatures as the veins evolved. Salinities likewise changed during vein evolution. The first mineralizing fluids introduced at the beginning of stage 2 were influenced by CO_2, giving them a lower average salinity than stage 3 fluids. As the fluids lost CO_2, they became more NaCl enriched, shown by an increase in average salinity for stage 3 mineralization (table 5). During stage 4, salinities decreased, with an increase in dissolved CO_2 causing carbonate minerals to become stable.

A total of 97 salinities from Tm ice plus Tm clathrate measurements are shown on a cumulative frequency plot (fig. 9). There are two salinity populations, a peak at 0–1 representing CO_2-enriched inclusions with a salinity that varies from 0 to 2.9 wt% NaCl equivalent, and a peak at 7–8 representing CO_2-depleted fluids that are NaCl enriched with a salinity that varies from 3.1 to 10.9 wt% NaCl equivalent. The inclusions from Tm ice measurements representing NaCl-enriched fluids have a general bell-shaped curve, implying the veins developed from a single fluid that was initially enriched in CO_2.

Eight inclusions from stage 2 consisted of water with carbon dioxide vapor and liquid. During heating experiments, the liquid and vapor CO_2 homogenized to vapor at a temperature range of 19.4°C to 28.9°C (table 6). Freezing experiments yielded a Tm for CO_2 (S) ranging from -55.8° to -58.5°C. An attempt was made to determine Th for liquid CO_2 and brine inclusions, but they decrepitated upon heating. A fibrous daughter mineral, dawsonite, was observed in some of the three phase inclusions. The identification was based on the fibrous physical characteristic, high birefringence (Zimmerman, 2016) and the association with CO_2-rich brines (Coveney and Kelly, 1971).

During the freezing runs of 25 inclusions, carbon dioxide hydrate or clathrate formed in the water or brine. From the 25 inclusions that developed clathrate, only four met the criteria used for salinity or NaCl wt% equivalent calculations (table 6). Salinity calculations are restricted to three phase inclusions, with both gas and liquid CO_2 in brine and $Tm_{clathrate}$ decomposition temperatures needing to be below 10°C (Collins, 1979). Salinities were calculated using the equation from Diamond (1992) by using $Tm_{clathrate}$ data for four inclusions with both liquid and vapor CO_2, and brine. From the calculations, salinities were deter-

Table 6. Data for 25 CO_2-enriched fluid inclusions.

Inclusion Type	Th°C CO_2 l to v Range	Th°C Range	Th°C Average	Tm°C Clathrate Range	Salinity Range	Salinity Average
CO_2 L+V+H_2O	19.4–28.9	299–317	308	10.2–11.6	0.0	0.0
H_2O+V+CO_2 in solution	NA	293–318	305	10.5–11.4	0.0	0.0
Brine+V+CO_2 in solution	NA	306–341	322	2.3–9.7	NA	NA
CO_2 L+V+brine	24.0–30.7	313–318	315	8.6–9.9	0.2–2.9	1.4

Note. From eight fluid inclusions with CO_2 liquid and vapor with water (CO_2 L+V+H_2O), two inclusions yielded homogenization temperatures. From four inclusions with water and CO_2 in solution with vapor (H_2O+V+CO_2 in solution), two inclusions yielded homogenization temperatures. From nine inclusions with brine and vapor with CO_2 in solution (brine+V+CO_2 in solution), seven inclusions yielded homogenization temperatures. Four inclusions with brine and CO_2 liquid and vapor (CO_2 L+V+brine) yielded salinity and Th results. Th°C temperature of homogenization in degrees centigrade. Tm°C temperature of melting in degrees centigrade. Salinity in wt% NaCl equivalent. NA, not applicable.

mined to be 0.2 to 2.9 wt% NaCl equivalent and averaged 1.4 wt% NaCl equivalent (table 6).

Experimental observations and a phase diagram developed by Collins (1979) indicate for $Tm_{clathrate}$ temperatures above 10°C the mass % NaCl in solution will be zero. Twelve inclusions had $Tm_{clathrate}$ temperatures above 10°C trapping NaCl free water with CO_2 liquid and vapor or dissolved carbon dioxide. Nine inclusions developed clathrate upon freezing with Tm temperatures below 10°C but did not have CO_2 liquid or vapor bubbles and therefore could not be used for salinity calculations (Collins, 1979). Upon heating, Th for 15 inclusions that did not decrepitate varied from 293°C to 341°C.

SULFUR ISOTOPES

Sulfur isotope compositions for 100 samples were analyzed at the stable isotope laboratory of the U.S. Geological Survey Crustal Geophysics and Geochemistry Science Center in Denver, Colorado. Analysis of sulfur isotopes was done by vacuum-line conversion to SO_2 followed by an elemental analyzer using a Thermo Delta Plus XP mass spectrometer. Samples were extracted under a microscope from cut slabs using a Dremel tool and diamond bit or were extracted by hand picking from specimens. All measured sulfur isotope values are reported in the standard $\delta^{34}S$‰ notation (in per mil, ‰) relative to the Canyon Diablo troilite (CDT) standard. The complete data set is shown in appendix D.

The cumulative frequency plots (fig. 10) show trends in the isotopic signatures within each mineralizing stage. Stage 2 pyrite had the highest detected $\delta^{34}S$ signature (8.7‰; fig. 10, table 7) and stage 3 galena had the lowest detected $\delta^{34}S$ signature (1.0‰; fig. 10, table 7). A trend shows pyrite that crystallized with arsenopyrite in stage 2 has a higher $\delta^{34}S$ signature than later pyrite that crystallized with sphalerite and galena in stage 3. Arsenopyrite and sphalerite crystallization overlap between stages and show similar $\delta^{34}S$ signatures (table 7). Galena has the lowest sulfur isotope signature.

Geothermometry was determined for isotope pairs from stage 3 mineralization using methods described by Ding and others (2003). Pyrite–galena pairs were not used for sulfur isotope geothermometry because pyrite precipitated over a wide range of the paragenetic sequence, overlapping mineralizing stages. Rye and Ohmoto (1974) noted pyrite and galena pairs seldom give reliable temperatures because pyrite precipitates throughout the paragenetic sequence. Sphalerite–galena pairs, showing co-genetic relationships and physical evidence of them being in equilibrium, were selected for geothermometry calculations. Isotopes from 15 different sphalerite–galena pairs representing most of the major veins in the district were used in the calculations and are summarized in appendix E. Results showed equilibrium temperatures ranged from 230°C to 476°C and averaged 340°C, overlapping fluid inclusion temperatures ranging from 127°C to 353°C.

DISCUSSION

Fluid inclusion and sulfur isotope data suggest the veins developed from an evolving hydrothermal fluid with a magmatic origin and were influenced by Proterozoic Belt Supergroup rocks. Sulfur isotopic compositions exceeding 8‰ are found in the Emery veins, but sulfur derived from a magmatic source such as a mantle-sourced basaltic magma would be expected to have an initial isotopic composition of 3‰ and for acidic igneous rocks to have 0 ± 3‰ (Ohmoto and Rye, 1979). To exceed the 3‰ sulfur isotopic composition, the magmatic fluid source needs to be enriched in $\delta^{34}S$ from assimilated crustal rocks. Magmatic assimilation of isotopically heavy marine evaporite sulfate would cause a $\delta^{34}S$ enrichment of a source magma (Field and others, 2005). Investigations by Claypool and others (1980) show Proterozoic and Phanerozoic marine evaporates are enriched in $\delta^{34}S$ ranging from 10‰ to 35‰, and could be a crustal source for heavy sulfur.

Sedimentary sulfide and/or evaporites from the middle Proterozoic Belt Supergroup were most likely the source of magmatic contamination through which the Boulder Batholith was emplaced (Harrison, 1972) and related intrusions. Evidence for Belt rocks being contaminants in intrusions underlying the Emery mining district is found in a granodiorite dike exposed in the district. Age dating of zircon from the granodiorite by U-Pb methods yielded a Proterozoic age of 1.77 Ga. The zircons are rimmed, indicating possible recrystallization when the granodiorite was intruded, but the rims are too narrow for age-dating analysis. In comparison, zircon from quartz porphyry dikes found in the Butte mining district also yield a Proterozoic age (1.5 to 2.5 Ga) and have narrow, Late Cretaceous rims (Lund and others, 2002; Field and others, 2005). The zircon ages from the quartz porphyry dikes at Butte are interpreted to be sourced from Belt rock being assimilated into the dikes (Field and others, 2005). The source intrusion for the granodiorite dike in the Emery mining district may have likewise assimilated

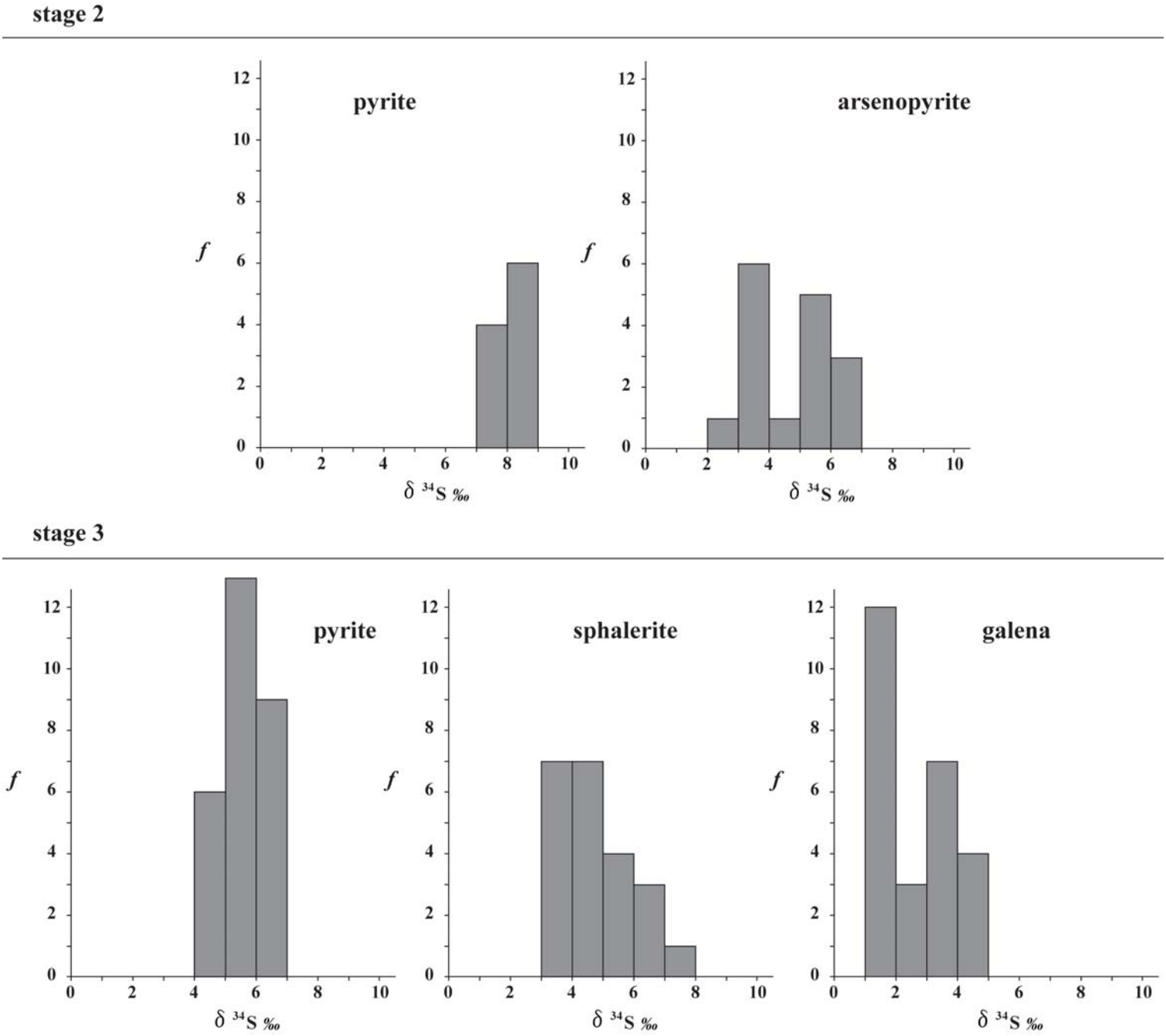

Figure 10. Cumulative frequency plots of sulfur isotope values (‰ relative to CDT standard) for sulfides from mineralizing stages 2 and 3. Complete data set is listed in appendix D.

Table 7. Summary of sulfur isotope analytical results. $\Delta^{34}S‰$ sulfur isotopes in parts per million.

Mineralizing Stage	Mineral	Number of Samples	$\Delta^{34}S‰$ Range	$\Delta^{34}S‰$ average
2	Pyrite	10	7.0–8.7	8.0
2	Arsenopyrite	14	2.0–6.4	4.8
3	Pyrite	28	4.0–6.8	5.5
3	Sphalerite	22	3.4–7.2	4.8
3	Galena	26	1.0–4.3	2.6

Belt rock, yielding Proterozoic zircon ages.

The Belt Missoula Group includes red bed siltstones and mudstones with salt casts, indicating a shallow marine to supratidal depositional environment (Smith and Barnes, 1966). Evaporite sulfate has not been found in Belt rocks, but the presence of salt casts in the Missoula Group suggests these supratidal deposits contained gypsum (Field and others, 2005). Barite with $\delta^{34}S$ of 13.6‰, 14.4‰, and 18.3‰ found in the Newland Formation is inferred to have replaced primary evaporitic gypsum and anhydrite (Strauss and Schieber, 1990). Diagenetic pyrite found in the Newland Formation has $\delta^{34}S$ values ranging from -8.7‰ to 36.7‰ with an average of 7.6‰ (Lyons and others, 2000). Isotopically heavy sulfur is found in sulfides from the Cu-Ag deposits, which are hosted by the Belt Supergroup located at Spar Lake. These deposits developed after early diagenesis when Cu-Ag-bearing hydrothermal fluids encountered reduced siltstones of the Revett Formation, causing the precipitation of Cu and Cu-Fe sulfides. The sulfides from this deposit have $\delta^{34}S$ values ranging from 3‰ to 23‰ (Hayes and Einaudi, 1986; Hayes and others, 1989).

Regional extent of the Belt Supergroup shows a relationship with the Boulder Batholith (Harrison, 1972) and could serve as potential contaminants for the Butte quartz porphyry magma (Field and others, 2005). Field and others (2005) suggests a Belt source for isotopically heavy sulfur would be sufficient to raise $\delta^{34}S_{\Sigma S}$ from a mantle value of 0‰ to a magmatic value of 10‰ when assimilated Belt Supergroup sulfur is combined and equilibrated with a subequal or lesser amount of magmatic sulfur. The same Belt Supergroup sulfur source may have caused the enrichment of the $\delta^{34}S$ values found in the Emery veins.

Mineralization took place from a hydrothermal fluid of two contrasting compositions: (1) those enriched in CO_2 with low salinities and (2) those lacking CO_2 enrichment with increased salinities. These two different types of hydrothermal fluids may have evolved from a single parental magmatic-derived fluid similar to that proposed by Reed and others (2013) for the Butte mining district.

Reed and others (2013) suggest the Butte mining district veins developed from a single parental magmatic-derived fluid of constant initial composition that underwent cooling, depressurization, wall-rock reactions, and fluid unmixing. Deep drilling of quartz veins in the Butte district revealed fluid inclusions with from 2 to 5 wt% NaCl and 2 to 8 mol percent CO_2 trapped at temperatures between 575°C and 650°C at a depth of 6 and 9 km. As these fluids ascended, they cooled and formed dark micaceous veins at moderate depths, pressures between 60 and 90 MPa, and at temperatures of about 600°C. At shallower depths, pale green sericite veins formed as the same fluid cooled to about 475°C with pressures between 50 and 70 MPa, unmixed, and reacted with wall rock (Rusk and others, 2008a).

Separation of a parental magmatic fluid into two fluid types can be caused by boiling or reactions with wall rock causing mineralization. Because evidence for boiling or effervescence was only found in stage 2 fluid inclusions and not found in stage 3 mineralization, phase separation caused by boiling or effervescence would be limited. Boiling will only take place when the veins fractured and brecciated from hydrostatic over-pressuring, thus limiting phase separation by this one event.

The change of a CO_2-enriched hydrothermal fluid to a fluid deficient in CO_2 results in a pH change from acidic to alkali (Reed and Palandri, 2006). The initial magmatic-derived fluids were enriched in CO_2 and would have an acidic pH. When these acidic hydrothermal fluids came in contact with host rock feldspar, they reacted, producing carbonate minerals and resulting in the loss of CO_2 and shifting the pH to alkaline (Reed and Palandri, 2006). Reed and Palandri (2006) further suggest a loss of CO_2 from boiling or effervescence will likewise result in a pH shift from acidic to alkaline.

As the first hydrothermal, low-salinity, CO_2-enriched fluid exsolved from a crystallizing pluton, it invaded fractures and faults, reacting with the basalt–andesite host rock, losing dissolved CO_2 and increasing in salinity. Temperature and pressure changes also caused the fluids to give up dissolved CO_2 along with wall-rock reactions. As a result of these physical changes, fluid unmixing took place, generating the moderate salinity hydrothermal fluids that created the polymetallic veins.

Pressure and Depth of Mineralization

The Emery veins are hosted by the lowest member of the Elkhorn Mountains Volcanics, which is estimated to be 4.6 km (2.9 mi) thick (Smedes, 1966). At this depth, the lithostatic pressure would be approximately 1.3 kilo bars (kbars) assuming a geobaric gradient of 3.5 km per kbar (Zimmerman, 2016).

Lithostatic pressure and depth of mineralization is estimated from the presence of three phase CO_2 inclusions. Most of the CO_2 inclusions homogenized to liquid CO_2 and had a density near 0.6 g/cm^3, with one

exception of 0.8 g/cm^3, and inclusions that homogenized to vapor CO_2 had a density that varied from 0.1 g/cm^3 to 0.3 g/cm^3 (Zimmerman, 2016). Zimmerman (2016) estimated the volume for homogenized CO_2 to occupy 40% to 70% of the total fluid inclusion volume. By plotting the final homogenization temperature and homogenized CO_2 volume on a diagram for a CO_2 density of 0.6 g/cm^3 and 0 wt% NaCl equivalent from Brown and Lamb (1989), a pressure range of 1.2 kbars to 1.7 kbars was obtained (Zimmerman, 2016). The trapping pressure estimate for the CO_2 inclusions straddles the pressure estimate 1.3 kbars for the thickness of the Elkhorn Mountain Volcanics. Fluid pressures exceeding lithostatic pressure could form low-angle veins by lifting the overlying rock along planes of weakness (Zimmerman, 2016). Hydrostatic pressures exceeding lithostatic pressures could also brecciate the host rock and early mineralizing stages during vein development, causing brecciation textures shown in figure 7A.

Pressure estimates were determined from aqueous fluid inclusions as well as CO_2 inclusions. Zimmerman (2016) used an average homogenization temperature of 264°C for aqueous inclusions and an average temperature of 340°C for isotope geothermometry of sphalerite–galena pairs. These temperatures were applied to a diagram by van den Kerkhof (2011) for a salinity of 5 wt% NaCl equivalent that yielded pressures of 1.1–1.2 kbars (Zimmerman, 2016). These pressures are close to the estimated lithostatic pressure based on the Elkhorn Mountains Volcanic thickness.

Temperature of Vein Formation

Average sulfur isotope geothermometry temperature (340°C) is 80°C higher than the average fluid inclusion temperature (260°C) for stage 3 mineralization. There is no evidence of boiling in stage 3 mineralization and all inclusions homogenized to liquid, indicating trapping above the liquid–vapor curve in the one phase field. Differences in sulfur isotope geothermometry and fluid inclusion homogenization temperatures could be attributed to lack of boiling in stage 3 mineralization.

To obtain the true fluid inclusion trapping temperature, an isochoric correction will need to be applied to the homogenization temperatures. From CO_2-enriched inclusions, stage 2 mineralization was determined to take place at pressures similar to stage 3 (Zimmerman, 2016), and the same temperature correction can be applied to both stages. The upper pressure limit is set by the total thickness of the Elkhorn Mountains Volcanics at 1.3 kbars. A fluid density of 0.75 g/cm^3 was determined from average salinity and Th for stage two mineralization (Roedder, 1984). By applying the lithostatic pressure and fluid density to a pressure temperature diagram from Fisher (1976), a temperature correction of 60°C was determined from the average sulfur isotope geothermometry temperature (340°C). Applying the 60°C correction to stage 2 fluid inclusions yielded an inferred trapping temperature ranging from 342°C to 414°C, with an average of 370°C, and stage 3 fluid inclusions yielded an inferred trapping temperature ranging from 283°C to 338°C, averaging 320°C.

Vein Genesis

From the fluid inclusion and isotopic data, it appears the veins developed from a single hydrothermal fluid that underwent chemical changes resulting from fluctuating temperatures, pressures, and host rock reactions. Pressure-corrected fluid inclusion data indicate the hydrothermal system ranged in temperature from 127°C to 476°C, with the upper temperatures from 353°C to 401°C being dominated by CO_2-enriched inclusions. Aqueous inclusions were found across the entire temperature range. Salinities ranged from 0.0 to 8.8 wt% NaCl equivalent for the aqueous inclusions and 0.0 to 2.9 wt% NaCl equivalent for the CO_2-enriched inclusions. As the early CO_2-enriched inclusions lost CO_2 they evolved into a denser brine solution.

The presence of low-salinity, carbon-dioxide-bearing inclusions is usually an indication of a magmatic-derived single-phase hydrothermal fluid (Rusk and others, 2008a). For the Emery mining district, carbon dioxide, low-salinity inclusions suggest a single-phase hydrothermal fluid was derived from a magmatic source at temperatures exceeding 400°C and a lithostatic pressure of 1.3 kbars and hydrostatic pressure up to 1.7 kbars.

Temperature and pressure variations, wall-rock reactions, and vein precipitation caused the fluids to evolve and chemically change (Rusk and others, 2008a). Ascending hydrothermal fluids invading fractures and faults reacted with the basalt–andesite wall rocks developing sericitic, argillic, carbonic, and silicic alteration. Wall-rock reactions in conjunction with physical changes caused the hydrothermal fluids to lose CO_2, increasing in salinity and evolving into fluids that became metal- and sulfur-enriched, transporting metals away from a magmatic source.

GEOLOGIC MODEL

A geologic model for the development of the polymetallic veins was derived from fluid inclusion, sulfur isotope, geophysical, and geologic data obtained from this investigation. The Emery mining district developed during continental arc magmatism that erupted the EMV. The EMV erupted in two cycles: an early effusive, dominantly andesite cone phase followed by a later, explosive, dominantly rhyolite, caldera phase. Age dating of the alteration related to the Emery veins shows a relationship with the later rhyolite caldera phase of the EMV. Sericite from altered granodiorite yielded a $^{40}Ar/^{39}Ar$ date of 77.93 ± 0.30 Ma; zircon from the EMV yielded U-Pb ages of 77.4 ± 0.8 Ma and 78.5 ± 1.6 Ma. A diorite intrusion hosted by Cretaceous sedimentary rocks within the EMV yielded a zircon U-Pb age of 79.8 ± 1.1 Ma. The ages of the youngest EMV formation (77.4 ± 0.8 Ma) and vein-related alteration (77.93 ± 0.30 Ma) suggest the Emery mining district formed near the close of the EMV eruption event.

Mineralization took place elsewhere in the Boulder Batholith during the same time period as the Emery mining district. At the Golden Sunlight mine, located in the southeast part of the batholith, an age ranging from 76.9 ± 0.5 Ma to 84.4 ± 2.1 Ma is reported by Oyer and others (2014) and DeWitt and others (1996) for the emplacement of the Golden Sunlight breccia pipe. This age range suggests the Golden Sunlight breccia pipe was emplaced during Elkhorn Mountains volcanism at the same time the Emery mining district was developed. Emplacement of the Golden Sunlight breccia pipe is related to alkali-calcic rhyolite of the EMV derived from deep crustal sources (DeWitt and others, 1996). Lamprophyre dikes cutting the breccia pipe are related to the EMV and were derived from a mantle source (Dewitt and others, 1996).

The veins in the Emery mining district developed on the margin of a caldera that erupted the EMV formations (plate 1). Near the close of volcanism, calderas are resurgently domed, with magmatic intrusions following the final eruptive cycles (Hayba and others, 1985; Lipman and others, 1976). These intrusions occur within the caldera or outside the caldera ring fracture. They provide the heat and fluids to drive a geothermal system that will lead to the development of hydrothermal veins (Hedenquist and others, 2000). The Emery mining district veins had a magmatic origin, and may have developed from the cooling and releasing of volatile components from an intrusive body adjacent to the district.

Monzodiorite and diorite intrusions with $^{40}Ar/^{39}Ar$ ages from 81 to 79 Ma were intruded into the lowest member of the EMV volcanic suite on the Ratio Mountain and Wilson Park 7.5' quadrangles (Olson and others, 2016). Adjacent to the Emery mining district, a similar intrusion could have been emplaced at depth into the EMV during the close of volcanism and caldera development. This intrusion could have served as a source of heat and hydrothermal fluids that drove the Emery mining district geothermal system. The intrusion could have originated from a magma chamber underlain by a mafic magmatic source that originated from the mantle (DeBari and Coleman, 1989). As the pluton was being emplaced, it assimilated crustal rocks consisting of Proterozoic Belt Supergroup lithologies. Crustal rocks assimilated into a mafic pluton could be a source of carbon dioxide, metals, and sulfur for hydrothermal fluids being expulsed from a cooling intrusive (Robertson and others, 2015).

Underlying the district and EMV is the younger 74.5 ± 0.9 Ma Butte granite of the Boulder Batholith (Lund and others, 2002). Emplacement of the Butte granite truncated the EMV caldera and intrusion that drove the Emery mining district geothermal system. The top of the intrusion remains and is inferred by two magnetic lows (Hanna and others, 1994; also plate 1). The altered top of the intrusion and adjacent host rock may have mineralized from hydrothermal fluids exsolving from the lower portions of the cooling intrusion and mafic magma source. This could be an exploration target.

EXPLORATION POTENTIAL

The Emery mining district may have exploration potential for a deep-seated porphyry or stockwork vein system. Based on the results from this study, the veins in the Emery mining district can be classified as deep epithermal or mesothermal (Ridge, 1972) and are related to a magmatic source. This magmatic source supplied the metals that developed the veins and is speculated to be a deep-seated porphyry or stockwork vein system adjacent to the district. Geophysical evidence consisting of two magnetic lows underlying the east and west margins of the district are interpreted to be altered intrusions by Hanna and others (1994); they describe the magnetic lows as being similar to those found in the Butte mining district. However, the magnetic lows in the Emery mining district cover half the area of those in the Butte mining district (25 km^2 vs. 50 km^2). If the magnetic lows are related to a porphyry, the porphyry would most likely

be smaller than in the Butte mining district.

Epithermal veins and, in deep systems, mesothermal veins are known to be related to porphyry systems (Chang and others, 2011; Cook and Bloom, 1990; Sillitoe, 2010). The relationship of the Butte mining district porphyry system to vein systems is well documented (Rusk and others, 2008a,b; Reed and others, 2013, and Houston and Dilles, 2013). The veins in the Emery mining district could likewise be related to a deep porphyry or stockwork vein system, but this still needs to be proven with deep drilling and detailed geophysical surveys.

Past drilling in the 1980s did not encounter a porphyry system or intrusive body because drilling was not to sufficient depth. Exploration was for shallow disseminated gold deposits hosted by near-surface altered rocks that can be mined by open pit methods. One deep drill hole extending to approximately 2,900 ft bottomed in andesite and was not drilled to sufficient depth to explore for a deep porphyry system (Al-Khirbash, 1982). In addition, this hole was collared between the two magnetic-low anomalies identified by Hanna and others (1994). Exploring for a deep porphyry system in the Emery mining district will require targeting the magnetic anomalies with more detailed geophysical surveys followed by deeper drilling than the early attempt of 2,900 ft. To test the hypothesis of a porphyry system or intrusion being related to the polymetallic veins will require drilling to depths exceeding 4,000 ft.

ACKNOWLEDGMENTS

We would like to give a special thank you to two outside reviewers, Mark Reed from the Department of Geological Sciences, University of Oregon, and Bob Houston from the Oregon Department of Geology and Mineral Industries for their time and effort reviewing the manuscript. They provided valuable suggestions and comments that greatly improved the final report. We also extend a special thanks to the patented claim owners who granted us permission to enter and sample the mines and prospects on their property. Without their cooperation and help, it would not have been possible to conduct this study. We would also like to thank the two MBMG reviewers, Katie McDonald and Phyllis Hargrave, and Chris Gammons, Department of Geological Engineering, Montana Tech of the University of Montana, whose comments and suggestions improved the final manuscript. Edited by Susan Barth, MBMG.

REFERENCES

Al-Khirbash, Salah, 1982, Geology and mineral deposits of the Emery mining district, Powell County, Montana: Missoula, University of Montana, M.S. thesis, 60 p.

Brannon, C.A., 1989, Hidden Hand project-final report: Freeport-McMoRan unpublished report, Montana Bureau of Mines and Geology archives, 15 p.

Brown, P.E., and Lamb, W.M., 1989, P-V-T properties of fluids in the system H_2O±CO_2±NaCl: New graphical presentations and implications for fluid inclusion studies: Geochimica et Cosmochimica Acta, v. 53, p. 1209–1221.

Burnham, C.W., 1985, Energy released in subvolcanic environments: Implications for breccia formation: Economic Geology, v. 80, p. 1515–1522.

Callaway, H.M., 1950, Mineralization of the Bonanza Mine: Butte, Montana School of Mines, B.S. thesis, 29 p.

Chang, Z., Hedenquist, J.W., White, N.C., Cooke, D.R., Roach, M., Deyell, C.L., Garcia, J. Jr., Gemmell, J.B., Stafford, M., and Cuison, L., 2011, Exploration tools for linked porphyry and epithermal deposits: Example from Mankayan intrusion-centered Cu-Au district, Luzon, Philippines: Economic Geology, v. 106, p. 1365–1398.

Claypool, G.E., Holser, W.T., Kaplan, I.R., Saki, H., and Zak, I., 1980, The age curves of sulfur and oxygen isotope in marine sulfate and their mutual interpretations: Chemical Geology, v. 28, p. 199–260.

Collins, P.L.F., 1979, Gas hydrates in CO_2-bearing fluid inclusions and the use of freezing data for estimation of salinity: Economic Geology, v. 74, p. 1435–1444.

Constenius, K.N., 1996, Late Paleogene extensional collapse of the Cordilleran foreland fold and thrust belt: Geological Society of America Bulletin, v. 108, p. 20–39.

Cooke, D.R., and Bloom, M.S., 1990, Epithermal and subjacent porphyry mineralization, Aupan, Baguio district, Philippines: A fluid-inclusion and paragenetic study: Journal of Geochemical Exploration, v. 35, p. 297–340.

Coveney, R.M., and Kelly, W.C., 1971, Dawsonite as a daughter mineral in hydrothermal fluid inclusions: Contributions to Mineralogy and Petrology, v. 32, p. 334–342.

DeBari, S.M., and Coleman, R.G., 1989, Examination of the deep levels of an island arc, the Tonsina ultramafic-mafic assemblage, Tonsina, Alaska: Journal of Geophysical Research, v. 94, p. 4373–4391.

Derkey, R.E., 1986, The Emery mining district, Powell County, Montana, in Lawson D.C., ed., Directory of Montana mining enterprises for 1985: Montana Bureau of Mines and Geology Bulletin 124, p. 31–42, 1:24,000 scale.

DeWitt, E., Foord, E.E., Zartman, R.E., Pearson, R.C., and Foster, F., 1996, Chronology of late Cretaceous igneous and hydrothermal events at the Golden Sunlight gold-silver breccia pipe, southwestern Montana: U.S. Geological Survey Bulletin 2155, 48 p.

Diamond, L.W., 1992, Stability of CO_2 clathrate hydrate + CO_2 liquid + CO_2 vapor + aqueous KCl-NaCl solutions: Experimental determination and application to salinity estimates of fluid inclusions: Geochimica et Cosmochimica Acta, v. 56, p. 273–280.

Ding, T., Zhang, C., Wan, D., Liu, Z., and Zhang, G., 2003, An experimental calibration on the sphalerite-galena sulfur isotope geothermometer: Acta Geologica Sinica, v. 77, no. 4, p. 519–521.

Dong, G., Morrison, G., and Jaireth, S., 1995, Quartz textures in epithermal veins, Queensland—Classification, origin, and implication: Economic Geology, v. 90, p. 1841–1856.

Elliott, H.C., 1939, The Emery mine, Powell County, Montana: Butte, Montana School of Mines, M.S. thesis, 45 p.

Elliott, J.E., Wallace, C.A., Lee, G.K., Antweiler, J.C., Lidke, D.J., Rowan, L.C., Hanna, W.F., Trautwein, C.M., Dwyer, J.L., and Moll, S.H., 1993, Maps showing mineral resource assessment for porphyry and stockwork deposits of copper, molybdenum, and tungsten and for stockwork and disseminated deposits of gold and silver in the Butte 1° x 2° quadrangle, Montana: U.S. Geological Survey Miscellaneous Investigations Series Map I-2050-F, map 1:250,000 and 1:500,000 scale and pamphlet, 30 p.

Field, C.W., Zhang, L., Dilles, J.H., Rye, R.O., and Reed, M.H., 2005, Sulfur and oxygen isotopic record in sulfate and sulfide minerals of early, deep main stage porphyry Cu-Mo and late main stage base-metal mineral deposits, Butte district, Montana: Chemical Geology, v. 215, p. 61–93.

Fisher, J.R., 1976, The volumetric properties of H_2O—A graphical portrayal: Journal of Research, U.S. Geological Survey, v. 4, no. 2, p. 189–193.

Foster, F., and Childs, J.F., 1993, An overview of significant lode gold systems in Montana, and their regional geologic setting: Exploration and Mining Geology, v. 2, p. 217–244.

Hanna, W.F., Hassemer, J.H., Elliott, J.E., Wallace, C.A. and Snyder, S.L., 1994, Maps showing gravity and aeromagnetic anomalies in the Butte 1° x 2° quadrangle, Montana: U.S. Geological Survey Miscellaneous Investigations Series Map I-2050-I, map 1:250,000 and 1:500,000 scale and pamphlet, 35 p.

Harrison, J.E., 1972, Precambrian Belt Basin of northwestern United States: Its geometry, sedimentation, and copper occurrences: Geological Society of America Bulletin, v. 83, p. 1215–1240.

Hayba, D.O., Bethke, P.M., Heald, P., and Foley, N.K., 1985, Geologic, mineralogic, and geochemical characteristics of volcanic-hosted epithermal precious-metal deposits, *in* Berger, B.R., and Bethke, P.M., eds., Geology and geochemistry of epithermal systems; Reviews in economic geology: Society of Economic Geologists, v. 2, p. 129–167.

Hayes, T.S., and Einaudi, M.T., 1986, Genesis of the Spar Lake strata-bound copper-silver deposit, Montana: Part I. Controls inherited from sedimentation diagenesis: Economic Geology, v. 81, p. 1899–1931.

Hayes, T.S., Rye, R.O., Whelan, J.F., and Landis, G.P., 1989, Geology and sulfur isotope geothermometry of the Spar Lake stratabound Cu-Ag deposit in the Belt Supergroup, Montana, in Boyle, R.W., Brown, A.C., Jowett, E.C., and Kirkham, R.V., eds., Sediment-hosted stratabound copper deposits: Geological Association of Canada Special Paper, v. 36, p. 319–338.

Hedenquist, J.W., Arribas, R.A., and Gonzalez-Urien, E., 2000, Exploration for epithermal gold deposits, in Hagemann, S.G., and Brown, P.E., eds., Gold in 2000; Reviews in Economic Geology: Society of Economic Geologists, v. 13, p. 245–277.

Hildebrand, R.S., 2013, Mesozoic assembly of the North American Cordillera: Geological Society of America Special Paper 495, 169 p.

Houston, R.A., and Dilles, J.H., 2013, Structural geological evolution of the Butte district, Montana: Economic Geology, v. 108, p. 1397–1424.

Joyce, J.P., 1951, A microscopic study of the ore minerals from the mines in the northern part of the Zosell (Emery) mining district: Butte, Montana School of Mines, B.S. thesis, 25 p.

Kennedy, A.K., Wotzlaw, J.F., Schalteger, U., Crowley, J.L., and Schmitz, M., 2014, Eocene zircon reference material for microanalysis of U-Th-Pb, isotopes and trace elements: Canadian Mineralogist, v. 52, p. 409–421.

Klepper, M.R., Weeks, R.A., and Ruppel, E.T., 1957, Geology of the southern Elkhorn Mountains, Jefferson and Broadwater Counties, Montana: U.S. Geological Survey Professional Paper 292, 82 p.

Lageson, Dave., Schmitt, J., Horton, B., Kalakay, T., and Burton, B., 2001, Influence of Late Cretaceous magmatism on the Servier orogenic wedge, western Montana: Geology, v. 29, p. 723–726.

Large, R.R., Gemmell, J.B., and Paulick, H., 2001, The alteration box plot: A simple approach to understanding the relationship between alteration mineralogy and lithogeochemistry associated with volcanic-hosted massive sulfide deposits: Economic Geology, v. 96, p. 957–971.

Lipman W.P., Fisher, F.S., Mehnert, H.H., Naeser, C.W., Luedke, R.G., and Steven, T.A., 1976, Multiple ages of mid-Tertiary mineralization and alteration in the western San Juan Mountains, Colorado: Economic Geology, v. 71, p. 571–588.

Lund, Karen, Aleinikoff, J.N., Kunk, M.J., Unhruh, D.M., Zeihen, G.D., Hodges, W.C., du Bray, E.A., and O'Neill, J.M., 2002, SHRIMP U-Pb and $^{40}Ar/^{39}Ar$ age constraints for relating plutonism and mineralization in the Boulder Batholith region, Montana: Economic Geology v. 97, p. 241–267.

Lyons, T.W., Luepke, J.J., Madeline, E.S., and Zieg, G.A., 2000, Sulfur geochemical constraints on Mesoproterozoic restricted marine deposition: Lower Belt Supergroup, northwestern United States: Geochimica et Cosmochimica Acta, v. 64, p. 427–437.

Mahoney, J.B., Pignotta, G.S., Ihinger, P.D., Wittkop, C., Balgord, E.A., Potter, J.J., and Leistikow, A., 2015, Geologic relationships in the northern Helena Salient, Montana: Geology of the Elliston Region: Northwest Geology, v. 44, p. 109–135.

Martin, Mark, Dilles, John, and Proffett, J.M., 1999, U-Pb geochronologic constraints for the Butte porphyry system: Geological Society of America Abstracts with Programs, v.31, no. 7, p. A380.

McClernan, H.G., 1976, Metallic mineral deposits of Powell County, Montana: Montana Bureau of Mines and Geology Bulletin 98, 69 p.

Nelson, C.E., and Giles, D.L., 1985, Hydrothermal eruption mechanisms and hot spring gold deposits: Economic Geology, v. 80, p. 1633–1639.

Ohmoto, H., and Rye, R.O., 1979, Isotopes of sulfur and carbon, *in* Barnes, H.L., ed., Geochemistry of hydrothermal ore deposits: 2nd edition, John Wiley and Sons, p. 509–567.

Olson, N.H., Dilles, J.H., Kallio, I.M., Horton, T.R., and Scarberry, K.C., 2016, Geologic map of the Ratio Mountain 7.5' quadrangle, southwest Montana: Montana Bureau of Mines and Geology EDMAP 10, scale 1:24,000.

Oyer, Nancy, Childs, J., and Mahoney, J.B., 2014, Regional setting and deposit geology of the Golden Sunlight mine: An example of responsible resource extraction, in Shaw, C.A., and Tikoff, B., eds., Exploring the Northern Rocky Mountains: Geological Society of America Field Guide 37, p. 115–144.

Pardee, J.T., and Schrader, F.C., 1933, Zosell (Emery) district, in Pardee, J.T., and Schrader, F.C. eds., Metalliferous deposits of the greater Helena mining region Montana: U.S. Geological Survey, Bulletin 842, p. 270–283.

Reed, M.H., and Palandri, J., 2006, Sulfide mineral precipitation from hydrothermal fluids, in Vaughan, D.J., ed., Sulfide mineralogy and geochemistry: Reviews in Mineralogy and Geochemistry, v. 61, p. 609–631.

Reed, M.H., Rusk, B., and Palandri, J., 2013, The Butte magmatic-hydrothermal system: One fluid yields all alteration and veins: Economic Geology, v. 108, p. 1379–1396.

Reynolds, M.W., 1979, Character and extent of Basin-Range faulting, western Montana and east-central Idaho, in Newman, G.W., and Goode, H.D., eds., Rocky Mountain Association of Geologists and Utah Geological Association Basin and Range Symposium, p. 185–193.

Ridge, J.D., 1972, Classification of ore deposits, in Ridge, J.D., ed., Annotated bibliographies of mineral deposits in the western hemisphere: Geological Society of America Memoir 131, p. 673–678.

Rivera, T.A., Storey, M., Schmitz, M.D., and Crowley, J.L., 2013, Age intercalibration of $^{40}Ar/^{39}Ar$ sani-

dine and chemically distinct U/Pb zircon populations from Alder Creek Rhyolite Quaternary geochronology standard: Chemical Geology, v. 345, p. 87–98.

Robertson, Forbes, 1953, Geology and mineral deposits of the Zosell (Emery) mining district, Powell County, Montana: Montana Bureau of Mines and Geology Memoir 34, 29 p., 5 plates.

Robertson, Jesse, Ripley, E.M., Barnes, S.J., and Li, Chusi, 2015, Sulfur liberation from country rocks and incorporation in mafic magmas: Economic Geology, v. 110, p. 1111–1123.

Roedder, Edwin, 1984, Fluid inclusions: Mineralogical Society of America, Reviews in Mineralogy, v. 12, 646 p.

Ruppel, E.T., 1961, Reconnaissance geologic map of the Deer Lodge quadrangle, Powell, Deer Lodge, and Jefferson Counties, Montana: U.S. Geological Survey Miscellaneous Field Studies Map MF-174, scale 1:48,000.

Rusk, B.G., Reed, M.H., and Dilles, J.H., 2008, Fluid inclusion evidence for magmatic-hydrothermal fluid evolution in the porphyry copper-molybdenum deposit at Butte, Montana: Economic Geology, v. 103, p. 307–334.

Rusk, B.G., Miller, B.J., and Reed, M.H., 2008a, Fluid inclusion evidence for the formation of main stage polymetallic base-metal veins, Butte, Montana, USA, in Spencer, J.E., and Titley, S.R., eds., Ores and orogenesis: Circum-Pacific Tectonics, Geologic Evolution, and Ore Deposits: Arizona Geological Society Digest 22, p. 573–581.

Rutland, E.T., Smedes, H., Tilling, R., and Greenwood, W., 1989, Volcanism and plutonism at shallow crustal levels: The Elkhorn Mountains Volcanics and the Boulder Batholith, southwestern Montana, *in* Henshaw, P., ed., Volcanism and plutonism of western North America; Volume 2, Cordilleran volcanism, plutonism, and magma generation at various crustal levels, Montana and Idaho, field trips for the 28th International Geological Congress: American Geophysical Union, Monograph, p. 16–31.

Rye, R.O., and Ohmoto, H., 1974, Sulfur and carbon isotopes and ore genesis: A review: Economic Geology, v. 69, p. 826–842.

Scarberry, K.C., 2016, Geologic map of the Sugarloaf Mountain 7.5' quadrangle, Deer Lodge, Powell and Jefferson Counties, Montana: Montana Bureau of Mines and Geology Open-File Report 674, scale 1:24,000.

Sillitoe, R.H., 1985, Ore-related breccias in volcanoplutonic arcs: Economic Geology, v. 80, p. 1467–1514.

Sillitoe, R.H., 2010, Porphyry copper systems: Economic Geology, v. 105, p. 3–41.

Smedes, H.W., 1966, Geology and igneous petrology of the northern Elkhorn Mountains, Jefferson and Broadwater Counties, Montana: U.S. Geological Survey Professional Paper 510, 82 p., scale 1:48,000.

Smith, A.G., and Barnes, W.C., 1966, Correlation of and facies changes in the carbonaceous, calcareous, and dolomitic formations of the Precambrian Belt-Purcell Supergroup: Geological Society of America Bulletin, v. 77, p. 1399–1426.

Stejer, F.A. Jr., 1948, The geology and ore deposition of the Bonanza mine, Emery (Zosel) mining district, Powell County, Montana: Butte, Montana School of Mines, M.S. thesis, 39 p.

Strauss, H., and Schieber, J., 1990, A sulfur isotope study of pyrite genesis: The mid-Proterozoic Newland Formation, Belt Supergroup, Montana: Geochimica et Cosmochimica Acta, v. 54, p. 197–204.

Tilling, R., Klepper, M., and Obradovich, J., 1968, K-Ar ages and time span of emplacement of the Boulder Batholith, Montana: American Journal of Science, v. 266, p. 671–689.

van den Kerkhof, A.M., 2011, Fluid inclusions-petrography and genetic interpretations of fluid inclusions: Geowissenschaftliches Zentrum der Universität Göttingen (Germany), short course, 44 p., http://www.uni-goettingen.de/de/26174.html [Accessed November 2016]

Zimmerman, J.L., 2016, Re-examination of ore-forming processes in the Emery mining district, Powell County, Montana: Butte, Montana Tech of the University of Montana, M.S. thesis, 127 p.

APPENDIX A

Description of Samples Used for U-Pb Zircon Dating

KCS-13-44—EMV rhyolitic ash flow tuff: CL-imaging of the zircons extracted from the tuff revealed predominantly luminescent crystals with only weak oscillatory and sector zoning, typical of volcanic zircons. A minority containing irregular non-luminescent cores were avoided in subsequent analysis. LA-ICP-MS affirmed the unimodal population of zircon and the lack of significant crystal inheritance; spot analyses of all 69 analyzed crystals yielded a normal distribution with a weighted mean 206Pb/238U date of 77.4 ± 0.8 (1.7) Ma (MSWD = 1.6).

KCS-13-28—EMV rhyolitic ash flow tuff (plate 1): Similar to sample KCS-13-44, CL-imaging of the zircons extracted from the tuff revealed predominantly luminescent crystals with only weak oscillatory and sector zoning, typical of volcanic zircons. In stark contrast to the other tuff, nearly every crystal from KCS-13-28 contains an irregular low-luminescent core. LA-ICP-MS analysis confirmed the ubiquity of inherited Proterozoic cores in these crystals. Twenty-eight spot analyses were rejected as biased by inherited cores on the basis of CL imagery and high within-run variance in U content and Pb/U ratio. The remaining 21 spot analyses yielded a normal distribution with a weighted mean $^{206}Pb/^{238}U$ date of 78.5 ± 1.6 (2.2) Ma (MSWD = 2.1). This result is within analytical error of sample KCS-13-44, suggesting that these are co-genetic magmatic products of the same caldera complex.

KCS-13-12—Diorite in fault zone: CL-imaging of the zircons extracted from the diorite revealed predominantly equant, weakly luminescent, oscillatory and sector-zoned crystals, with a minority of highly luminescent grains. LA-ICP-MS analysis confirmed that the luminescent crystals are Proterozoic. Ten spot analyses were rejected as biased by inherited cores on the basis of CL imagery and high within-run variance in U content and Pb/U ratio. The remaining 31 spot analyses yielded a normal distribution with a weighted mean $^{206}Pb/^{238}U$ date of 79.8 ± 1.1 (1.9) Ma (MSWD = 2.0).

E-25—Granodiorite dike from prospect trench in Emery mining district (plate 1): CL-imaging of the zircons extracted from this granodiorite revealed equant to elongate, relatively large, predominantly weakly luminescent, oscillatory-zoned crystals (fig. 2). Many crystals are decorated by a very thin (just few micrometer thickness), highly luminescent rim. All 41 spot analyses yielded a normal distribution with a weighted mean $^{207}Pb/^{206}Pb$ date of 1,777 ± 8(20) Ma (MSWD = 3.8). Excluding 10 analyses with discordance >5%, an equivalent weighted mean $^{206}Pb/^{238}U$ date of 1,771 ± 17 (25) Ma (MSWD = 2.0) was obtained. This result suggests a Paleoproterozoic crystallization age for this granodiorite. The very bright rims on the crystals may be a cryptic record of minor recrystallization of this granodiorite, but these domains are not accessible for analysis.

APPENDIX B

Whole-Rock Analysis of Alteration Types

Analytical results are given in percent and normalized to 100%. Results do not add to 100% due to rounding. Altered rock types are basaltic andesite except for samples E-25 and E-26, which is granodiorite. Samples KCS-13-18, KCS-13-22, and KCS-13-24 are from Scarberry's (2016) investigation of the Sugarloaf Mountain quadrangle. Samples R-1 to R-5 are from Robinson (1953). Dashed lines are oxides that were not analyzed.

Sample	Alteration	SiO_2	Al_2O_3	Fe_2O_3	CaO	MgO	Na_2O	K_2O	TiO_2	MnO	P_2O_5
E-3	Argillic	61.0	10.5	9.1	7.7	2.6	0.04	3.1	0.57	4.5	0.27
E-7	Argillic	63.2	14.3	10.4	2.4	3.7	0.51	4.0	0.76	0.2	0.4
E-25	Propylitic	66.0	16.6	5.7	2.2	1.7	3.4	2.9	0.6	0.07	0.25
E-26	Sericitic	72.6	15.9	4.1	0.08	0.76	0.14	4.8	0.62	0.01	0.14
E-38	Argillic	60.0	13.2	9.6	7.3	3.6	0.04	4.3	0.72	0.78	0.35
E-43	Sericitic	65.8	18	5.4	0.77	0.65	1.3	6.7	0.71	0.04	0.39
E-48	Silicic	73.5	11.3	10	0.28	0.57	0.03	3.4	0.58	0.01	0.12
E-63	Argillic	57.8	14.8	7.5	8.3	4.6	0.07	4.9	0.80	0.53	0.38
E-65	Carbonic	68.6	7.7	6.8	8.9	4.6	0.02	2.3	0.4	0.48	0.18
E-66	Silicic	69.8	17.2	2.5	0.44	0.96	5.2	2.3	1.1	0.01	0.08
E-67	Sericitic	60.9	15.8	10.1	0.99	4.5	1.6	4.2	0.84	0.23	0.44
E-68	Carbonic	56.6	15.5	7.9	8.2	5.2	0.99	4.2	0.84	0.24	0.39
E-69	Argillic	60.7	15.8	8.4	4.1	4.8	2.0	2.9	0.86	0.19	0.43
KCS-13-18	Argillic	53.5	15.8	8.7	5.8	8.5	2.2	4.0	0.93	0.25	0.48
KCS-13-22	Propylitic	55.6	15.7	9.1	6.6	5.1	3.3	3.2	0.87	0.14	0.39
KCS-13-24	Propylitic	57.4	18	6.7	4.5	4	3.3	4.9	0.91	0.08	0.49
R-1	Carbonic	56.7	15.7	9.4	8.8	5.0	2.5	1.5	0.66	------	------
R-2	Propylitic	56.0	15.8	9.1	7.7	4.5	2.9	2.6	0.65	------	------
R-3	Carbonic	49.8	14.5	10.9	11.2	7.5	2.9	1.5	1.3	------	------
R-4	Propylitic	56.2	12.1	10.4	9.6	2.6	5.1	3.7	0.56	------	------
R-5	Propylitic	56.8	15.8	8.6	7.7	4.9	1.5	2.8	0.89	0.36	0.09

APPENDIX C

Summary of Fluid Inclusion Data

Th_{CO2}, average temperature of CO_2 homogenizing to vapor; $Th_{CO2}l$, average temperature of CO_2 homogenizing to liquid; $Tm_{clathrate}$, average melting temperature for clathrate; Tm_{ice}, average melting temperature for ice; salinity given as wt % NaCl equivalent; Th, vapor to liquid homogenization temperature. All temperatures given in °C. Some CO_2-enriched inclusions formed both clathrate and ice. Data set from Zimmerman (2016).

Sample No.	Location	$Th_{CO2}v$	$Th_{CO2}l$	$Tm_{clathrate}$	Tm_{ice}	Salinity	Th
E-1	Hidden Hand		28.8	11.5		0.0	
E-1	Hidden Hand		29.5	11.2		0.0	
E-1	Hidden Hand		28.0	11.2		0.0	
E-1	Hidden Hand		28.5	11.6		0.0	
E-1	Hidden Hand		28.4	11.2		0.0	
E-1	Hidden Hand				-4.2	6.7	284.8
E-1	Hidden Hand				-2.8	4.6	282.2
E-1	Hidden Hand				-4.7	7.4	335.9
E-1	Hidden Hand				-4.7	7.4	335.9
E-1	Hidden Hand				-4.6	7.2	332.0
E-1	Hidden Hand				-5.5	8.5	339.3
E-1	Hidden Hand				-4.8	7.6	347.7
E-1	Hidden Hand						342.5
E-1	Hidden Hand			7.4	-3.5	5.7	341.1
E-1	Hidden Hand			2.3	-5.7	8.8	337.1
E-1	Hidden Hand						327.5
E-1	Hidden Hand			5.4	-4.0	6.4	
E-1	Hidden Hand				-4.7	7.4	341.8
E-1	Hidden Hand			10.8	-4.4	7.0	
E-1	Hidden Hand			11.1	-4.4	7.0	293.1
E-1	Hidden Hand			11.2	-4.7	7.4	317.6
E-1	Hidden Hand				-4.4	7.0	296.4
E-1	Hidden Hand			9.6			306.3
E-1	Hidden Hand				-4.7	7.4	286.3
E-1	Hidden Hand				-5.5	8.5	292.6
E-1	Hidden Hand		30.7	9.9		0.2	317.9
E-1	Hidden Hand		19.5	10.7	-3.3	5.4	298.9
E-1	Hidden Hand						316.2
E-1	Hidden Hand						327.5
E-1	Hidden Hand			9.7	-0.3	0.6	189.2
E-1	Hidden Hand						289.3
E-1	Hidden Hand				-3.6	5.8	276.8
E-1	Hidden Hand				-3.2	5.3	283.9
E-3	Blue-Eyed Maggie				-4.2	6.8	204.7
E-3	Blue-Eyed Maggie				-4.6	7.2	236.4
E-3	Blue-Eyed Maggie				-3.8	6.2	209.2
E-3	Blue-Eyed Maggie				-1.8	3.1	
E-3	Blue-Eyed Maggie				-3.7	6.0	171.8
E-3	Blue-Eyed Maggie				-3.4	5.5	186.7
E-3	Blue-Eyed Maggie				-2.8	4.7	190.1
E-3	Blue-Eyed Maggie				-2.9	4.7	169.0

Sample No.	Location	$Th_{CO2}v$	$Th_{CO2}l$	$Tm_{clathrate}$	Tm_{ice}	Salinity	Th
E-3	Blue-Eyed Maggie				-3.5	5.7	197.1
E-3	Blue-Eyed Maggie				-1.8	3.1	127.4
E-8	Emma Darling						215.0
E-8	Emma Darling				-4.2	6.7	188.5
E-8	Emma Darling				-5.0	7.9	170.9
E-8	Emma Darling				-4.9	7.7	196.3
E-8	Emma Darling				-3.2	5.2	
E-8	Emma Darling				0.0	0.0	353.7
E-14	Hidden Hand		27.5	11.2		0.0	245.0
E-14	Hidden Hand		29.8	10.9		0.0	
E-14	Hidden Hand		28.4	10.3		0.0	
E-14	Hidden Hand		28.1	10.9		0.0	301.9
E-14	Hidden Hand		29.4	11.0		0.0	
E-14	Hidden Hand		28.2	11.2		0.0	301.9
E-14	Hidden Hand				-4.3	6.9	245.8
E-14	Hidden Hand		27.8	11.2		0.0	
E-14	Hidden Hand		27.1	11.2		0.0	
E-14	Hidden Hand				-4.6	7.2	247.0
E-23	Argus				-4.4	7.1	238.8
E-23	Argus				-3.2	5.2	132.0
E-23	Argus						252.0
E-23	Argus				-3.1	5.1	
E-23	Argus				-4.3	6.9	240.7
E-23	Argus				-3.3	5.3	234.1
E-23	Argus				-2.8	4.6	214.8
E-23	Argus				-3.4	5.5	204.5
E-23	Argus						205.1
E-23	Argus				-3.4	5.5	189.4
E-27	Elizabeth				-4.4	7.1	308.9
E-27	Elizabeth				-3.9	6.2	281.5
E-27	Elizabeth				-4.3	6.9	
E-27	Elizabeth						170.0
E-27	Elizabeth				-4.2	6.7	
E-27	Elizabeth				-4.1	6.6	
E-27	Elizabeth				-5.0	7.9	307.1
E-27	Elizabeth				-4.8	7.6	314.7
E-27	Elizabeth						309.9
E-27	Elizabeth				-4.3	6.9	184.7
E-27	Elizabeth				-3.5	5.7	
E-27	Elizabeth				-4.3	6.9	
E-27	Elizabeth				-4.7	7.4	203.9
E-27	Elizabeth				-4.5	7.1	277.2
E-35	Emery				-7.3	10.9	
E-35	Emery				-3.3	5.4	
E-35	Emery				-3.9	6.3	324.3
E-35	Emery						314.7
E-35	Emery						317.4

Sample No.	Location	$Th_{CO2}v$	$Th_{CO2}l$	$Tm_{clathrate}$	Tm_{ice}	Salinity	Th
E-35	Emery						308.8
E-35	Emery						205.2
E-35	Emery						319.2
E-35	Emery						319.2
E-35	Emery						222.7
E-35	Emery						193.2
E-35	Emery						306.8
E-35	Emery						322.1
E-35	Emery						300.0
E-35	Emery						219.2
E-35	Emery						314.7
E-35	Emery						316.9
E-35	Emery						338.5
E-35	Emery						276.3
E-35	Emery						322.5
E-35	Emery				-3.4	5.5	
E-61	Paymaster				-0.7	1.2	314.6
E-61	Paymaster						303.4
E-61	Paymaster				-2.4	4.0	
E-61	Paymaster				-2.7	4.5	313.0
E-61	Paymaster				-2.9	4.7	
E-61	Paymaster	28.2		9.7		0.6	313.1
E-61	Paymaster				-4.5	7.2	313.1
E-61	Paymaster	25.7		9.2		1.6	313.1
E-61	Paymaster	25.7			-5.6	8.7	317.1
E-61	Paymaster	24.0		8.6		2.9	313.5
E-61	Paymaster				-0.2	0.4	330.2
E-61	Paymaster				-5.4	8.4	322.7
E-61	Paymaster						214.8
E-70	Emery				-4.6	7.3	255.0
E-70	Emery				-4.4	7.0	
E-70	Emery				-4.4	7.0	251.0
E-70	Emery				-4.9	7.7	258.0
E-70	Emery				-4.6	7.3	254.0
E-70	Emery				-4.4	7.0	
E-70	Emery				-5.2	8.2	
E-70	Emery				-5.4	8.4	
E-70	Emery				-4.1	6.6	259.0
E-70	Emery						262.0
E-70	Emery						278.0
E-70	Emery						263.0
E-70	Emery						238.0
E-70	Emery						262.0
E-70	Emery						278.0
E-70	Emery						263.0
E-70	Emery						238.0
E-70	Emery						262.0
E-70	Emery						260.0
E-70	Emery						239.0

Sample No.	Location	$Th_{CO2}v$	$Th_{CO2}l$	$Tm_{clathrate}$	Tm_{ice}	Salinity	Th
E-70	Emery						261.0
E-70	Emery						257.0
E-70	Emery						254.0
E-70	Emery						285.0
E-70	Emery						283.0
E-70	Emery						164.0
E-70	Emery						261.0
E-70	Emery						264.0
E-70	Emery						230.0
E-70	Emery						264.0
E-70	Emery						241.0
E-70	Emery						261.0
E-70	Emery						261.0
E-70	Emery				-3.2	5.2	176.0
E-70	Emery						288.0
E-70	Emery				-3.3	5.3	190.0
E-70	Emery				-4.9	7.8	289.0
E-70	Emery				-3.2	5.2	197.0
E-70	Emery				-4.1	6.6	230.0
E-70	Emery				-2.9	4.8	
E-70	Emery						292.0
E-70	Emery				-2.8	4.7	
E-70	Emery				-2.8	4.7	
E-70	Emery						290.0
E-70	Emery						283.0
E-70	Emery						237.0
E-70	Emery						196.0
E-70	Emery						137.0
E-70	Emery						194.0
E-70	Emery						284.0
E-70	Emery						190.0
E-70	Emery						290.0
E-70	Emery						298.0
E-70	Emery						288.0

APPENDIX D

APPENDIX D

Summary of Sulfur Isotope Data

Sulfur isotope results are reported in the standard notation $\delta^{34}S‰$ relative to the Canyon Diablo Troilite standard.

Sample No.	Location	Mineral	Sample Description	$\Delta^{34}S‰$
E-1-1PY	Hidden Hand	Pyrite	Pyrite associated with quartz veining	5.4
E-2-1SP	Emma Darling	Sphalerite	Massive sulfide vein in altered basalt andesite	4.5
E-2-1PY	Emma Darling	Pyrite	Massive sulfide vein in altered basalt andesite	5.4
E-2-1AP	Emma Darling	Arsenopyrite	Massive sulfide vein in altered basalt andesite	3.4
E-4-1PY	Emma Darling	Pyrite	Disseminated pyrite in altered basalt andesite	8.7
E-5-1GL	Emma Darling	Galena	Massive sulfide vein in altered basalt andesite	4.1
E-5-1SP	Emma Darling	Sphalerite	Massive sulfide vein in altered basalt andesite	5.5
E-6-1PY	Emma Darling	Pyrite	Quartz with sulfide veining	6.2
E-6-1SP	Emma Darling	Sphalerite	Quartz with sulfide veining	4.3
E-7-1PY	Black Eyed May	Pyrite	Disseminated pyrite in altered basalt andesite	8.5
E-12-1GL	Hidden Hand	Galena	Quartz with disseminated sulfides	3.8
E-12-1PY	Hidden Hand	Pyrite	Quartz with disseminated sulfides	6.0
E-13-1PY	Hidden Hand	Pyrite	Disseminated sulfides in quartz veins	4.4
E-13-1GL	Hidden Hand	Galena	Disseminated sulfides in quartz veins	1.7
E-14-1PY	Hidden Hand	Pyrite	Massive sulfide vein with quartz veining	4.3
E-14-1SP	Hidden Hand	Sphalerite	Massive sulfide vein with quartz veining	3.6
E-14-1GL	Hidden Hand	Galena	Massive sulfide vein with quartz veining	1.7
E-21-1PY	Argus no. 6 adit	Pyrite	Disseminated sulfides in quartz veins	7.1
E-21-1SP	Argus no. 6 a	Sphalerite	Disseminated sulfides in quartz veins	5.6
E-21-1GL	Argus no. 6 adit	Galena	Disseminated sulfides in quartz veins	3.5
E-22-1PY	Hidden Hand	Pyrite	Quartz veins with disseminated sulfides	5.3
E-22-2GL	Hidden Hand	Galena	Quartz veins with disseminated sulfides	3.0
E-22-2PY	Hidden Hand	Pyrite	Quartz veins with disseminated sulfides	5.6
E-22-2AP	Hidden Hand	Arsenopyrite	Quartz veins with disseminated sulfides	5.5
E-24-1SP	Elizabeth	Sphalerite	Quartz veins with disseminated sulfides	5.6
E-24-1GL	Elizabeth	Galena	Quartz veins with disseminated sulfides	3.8
E-24-2PY	Elizabeth	Pyrite	Quartz veins with disseminated sulfides	5.3
E-24-2GL	Elizabeth	Galena	Quartz veins with disseminated sulfides	4.1
E-27-1SP	Elizabeth	Sphalerite	Disseminated sulfides and quartz veins	3.9
E-27-1GL	Elizabeth	Galena	Disseminated sulfides and quartz veins	1.9
E-27-1PY	Elizabeth	Pyrite	Disseminated sulfides and quartz veins	4.3
E-28-1SP	Bonanza	Sphalerite	Massive sulfide vein with quartz veining	4.3
E-28-1GL	Bonanza	Galena	Massive sulfide vein with quartz veining	3.9
E-28-1PY	Bonanza	Pyrite	Massive sulfide vein with quartz veining	4.3
E-29-1AP	Bonanza	Arsenopyrite	Disseminated arsenopyrite in quartz veins	6.4
E-31-1PY	Bonanza	Pyrite	Disseminated sulfides with quartz veins	4.0
E-31-2SP	Bonanza	Sphalerite	Disseminated sulfides with quartz veins	3.5
E-31-2GL	Bonanza	Galena	Disseminated sulfides with quartz veins	1.3
E-31-3AP	Bonanza	Arsenopyrite	Disseminated sulfides with quartz veins	5.6
E-32-1Gl	Emery	Galena	Quartz veins and disseminated sulfides	1.1

Sample No.	Location	Mineral	Sample Description	$\Delta^{34}S‰$
E-32-1SP	Emery	Sphalerite	Quartz veins and disseminated sulfides	4.1
E-32-1AP	Emery	Arsenopyrite	Quartz veins and disseminated sulfides	2.0
E-32-1PY	Emery	Pyrite	Quartz veins and disseminated sulfides	4.8
E-32-2PY	Emery	Pyrite	Quartz veins and disseminated sulfides	5.1
E-32-2GL	Emery	Galena	Quartz veins and disseminated sulfides	1.9
E-32-2SP	Emery	Sphalerite	Quartz veins and disseminated sulfides	3.4
E-32-3PY	Emery	Pyrite	Quartz veins and disseminated sulfides	5.2
E-32-3GL	Emery	Galena	Quartz veins and disseminated sulfides	1.7
E-32-4PY	Emery	Pyrite	Quartz veins and disseminated sulfides	5.8
E-32-4AP	Emery	Arsenopyrite	Quartz veins and disseminated sulfides	3.8
E-33-1AP	Emery	Arsenopyrite	Asenopyrite crystals etched from calcite	5.7
E-33-2PY	Emery	Pyrite	Disseminated sulfides in quartz veins	6.3
E-33-2SP	Emery	Sphalerite	Disseminated sulfides in quartz veins	5.4
E-33-2AP	Emery	Arsenopyrite	Disseminated sulfides in quartz veins	5.6
E-37-1PY	Emery	Pyrite	Massive sulfides with quartz veins	6.8
E-37-1GL	Emery	Galena	Massive sulfides with quartz veins	1.7
E-37-1AP	Emery	Arsenopyrite	Massive sulfides with quartz veins	4.8
E-37-2SP	Emery	Sphalerite	Massive sulfides with quartz veins	4.6
E-37-3SP	Emery	Sphalerite	Massive sulfides with quartz veins	6.4
E-37-3GL	Emery	Galena	Massive sulfides with quartz veins	2.2
E-37-3AP	Emery	Arsenopyrite	Massive sulfides with quartz veins	5.2
E-40-1PY	Emery	Pyrite	Sulfides with carbonate and quartz veins	6.4
E-40-1GL	Emery	Galena	Sulfides with carbonate and quartz veins	2.1
E-40-1SP	Emery	Sphalerite	Sulfides with carbonate and quartz veins	4.3
E-42-1PY	Emery	Pyrite	Sulfides in altered basaltic andesite	7.0
E-42-1GL	Emery	Galena	Sulfides in altered basaltic andesite	1.8
E-42-1SP	Emery	Sphalerite	Sulfides in altered basaltic andesite	4.7
E-42-2AP	Emery	Arsenopyrite	Sulfides in altered basaltic andesite	6.4
E-44-1PY	Sterret	Pyrite	Sulfides in silicified basaltic andesite	7.0
E-44-1SP	Sterret	Sphalerite	Sulfides in silicified basaltic andesite	6.1
E-44-1GL	Sterret	Galena	Sulfides in silicified basaltic andesite	3.3
E-44-2AP	Sterret	Arsenopyrite	Sulfides in silicified basaltic andesite	6.3
E-46-1GL	Monday	Galena	Sulfides in altered basaltic andesite	4.1
E-46-1SP	Monday	Sphalerite	Sulfides in altered basaltic andesite	6.4
E-46-1PY	Monday	Pyrite	Sulfides in altered basaltic andesite	8.1
E-47-1PY	Monday	Pyrite	Sulfides in altered basaltic andesite	5.9
E-47-1SP	Monday	Sphalerite	Sulfides in altered basaltic andesite	7.2
E-48-1PY	Monday	Pyrite	Altered basaltic andesite, disseminated pyrite	6.7
E-49-1GL	Monday	Galena	Disseminated sulfides, altered basaltic andesite	4.3
E-49-1PY	Monday	Pyrite	Disseminated sulfides, altered basaltic andesite	6.7
E-51-1GL	Wednesday	Galena	Quartz veins, altered basaltic andesite, sulfides	3.7
E-51-1PY	Wednesday	Pyrite	Quartz veins, altered basaltic andesite, sulfides	7.3
E-51-2PY	Wednesday	Pyrite	Quartz veins, altered basaltic andesite, sulfides	6.4

Sample No.	Location	Mineral	Sample Description	$\Delta^{34}S‰$
E-53-1PY	Wednesday	Pyrite	Argillicly altered basaltic andesite with pyrite	8.8
E-55-1GL	Paymaster	Galena	Quartz vein with disseminated sulfides	1.3
E-55-1PY	Paymaster	Pyrite	Quartz vein with disseminated sulfides	5.7
E-55-2SP	Paymaster	Sphalerite	Quartz vein with disseminated sulfides	3.4
E-55-2GL	Paymaster	Galena	Quartz vein with disseminated sulfides	1.0
E-55-2PY	Paymaster	Pyrite	Quartz vein with disseminated sulfides	5.5
E-55-2AP	Paymaster	Arsenopyrite	Quartz vein with disseminated sulfides	3.1
E-56-1SP	Paymaster	Sphalerite	Quartz vein with disseminated sulfides	3.9
E-56-1AP	Paymaster	Arsenopyrite	Quartz vein with disseminated sulfides	3.6
E-56-1GL	Paymaster	Galena	Quartz vein with disseminated sulfides	1.9
E-56-1PY	Paymaster	Pyrite	Quartz vein with disseminated sulfides	5.9
E-62-1GL	Paymaster	Galena	Quartz veins with disseminated sulfides	1.3
E-62-1PY	Paymaster	Pyrite	Quartz veins with disseminated sulfides	5.1
E-62-2SP	Paymaster	Sphalerite	Quartz veins with disseminated sulfides	3.8
E-62-2GL	Paymaster	Galena	Quartz veins with disseminated sulfides	2.3
E-65-1PY	Paymaster	Pyrite	Altered basalt with disseminated pyrite	8.6
E-67-1PY	prospect pit	Pyrite	Amygdaloidal basalt, pyrite in amygduals	6.5
E-68-1PY	prospect pit	Pyrite	Amygdaloidal basalt, disseminated pyrite	8.6

APPENDIX E

Isotope pairs used for equilibrium temperature calculations using methods described by Ding and others (2003).

Sample No.	Location	Mineral Pair	$\delta^{34}S$‰	Temperature °C
E-5	Emma Darling	Galena	4.1	475.6
		Sphalerite	5.5	
E-14	Hidden Hand	Galena	1.7	364.5
		Sphalerite	3.6	
E-21	Argus tunnel no.6	Galena	3.5	332.1
		Sphalerite	5.6	
E-24	Elizabeth	Galena	3.8	382.8
		Sphalerite	5.6	
E-27	Elizabeth	Galena	1.9	347.7
		Sphalerite	3.9	
E-31	Bonanza	Galena	1.3	317.7
		Sphalerite	3.5	
E-32	Emery	Galena	1.1	230.3
		Sphalerite	4.1	
E-32	Emery	Galena	1.9	448.7
		Sphalerite	3.4	
E-40	Emery	Galena	2.1	317.7
		Sphalerite	4.3	
E-42	Emery	Galena	1.8	239.1
		Sphalerite	4.7	
E-44	Sterret	Galena	3.3	248.4
		Sphalerite	6.1	
E-46	Monday	Galena	4.1	304.2
		Sphalerite	6.4	
E-55	Paymaster	Galena	1.0	291.6
		Sphalerite	3.4	
E-56	Paymaster	Galena	1.9	347.7
		Sphalerite	3.9	
E-62	Paymaster	Galena	2.3	448.7
		Sphalerite	3.8	


MBMG
Montana Bureau of Mines and Geology